FABRICATION AND CHARACTERIZATION OF A QUANTUM DOT-SENSITIZED SOLAR CELL

by

Kevin J. Emmett

Thesis

Submitted to the Faculty of the

Graduate School of Vanderbilt University

in partial fulfillment of the requirements

for the degree of

MASTER OF SCIENCE

in

Physics

August, 2009

Nashville, Tennessee

Approved:

Sandra J. Rosenthal

Sharon M. Weiss

ABSTRACT

The design and characterization of a photovoltaic device employing CdSe nanocrystals sensitized to TiO_2 nanotubes is described. The project was divided into three major objectives: (1) fabrication of anodically-oxidized, highly-ordered TiO_2 nanotube arrays, (2) deposition of CdSe nanocrystals onto the nanotube arrays, and (3) construction of an all solid-state photovoltaic from these components. Characterization at each stage was conducted using a variety of techniques to determine structure, elemental composition, and device performance. The final product was a robust, working photovoltaic device with a measured efficiency of 0.015%.

ACKNOWLEDGEMENTS

TABLE OF CONTENTS

LIST OF TABLES

LIST OF FIGURES

CHAPTER I

INTRODUCTION

1.1   Introduction

Faced with the prospect of depleting oil supplies and the certainty of global climate change,[1] we are compelled to seek alternative sources to supply our growing energy demands. Several clean energy technologies will play an important role in this challenge, including wind, geothermal, biomass, hydroelectric, and nuclear. However, none of these technologies has the scalable capacity to meet the whole of our global energy demand. Only the sun, with its virtually limitless supply of fusion energy, can meet our energy needs. For a sense of scale, consider: the sun provides power to the earth at a rate of 130 TW. Current global energy consumption occurs at a rate of 13.5 TW, projected to rise to 40.8 TW in 2050. Today, in just one hour, the sun provides enough power to supply our energy needs for an entire year.[2] Accessing and utilizing this vast quantity of energy represents a grand challenge in scientific research and engineering.[3] Current silicon technologies have thus far experienced limited deployment, primarily due to materials costs associated with processing of the high quality crystalline silicon used in these devices. Developing cost-effective methods of efficiently capturing solar energy is urgently required.

This thesis describes the design, fabrication, and characterization of a photovoltaic device architecture employing semiconductor nanocrystals, a class of nanoscale material with unique physical properties well-suited for advanced photovoltaics. The discussion is organized as follows. The remainder of Chapter 1 provides a summary of relevant nanocrystal and photovoltaic physics, and introduces the device design. Chapter 2 describes the experimental device fabrication and characterization. Chap-

ter 3 details the fabrication of higly-ordered arrays of TiO_2 nanotubes. Chapter 4 describes the combination of CdSe nanocrystals and TiO_2 nanotubes into a photovoltaic device, and provides discussion of device performance and possible improvements. Chapter 5 summarizes the project conclusions and future directions. Two appendices outline related work undertaken during the course of the project.

1.2 Semiconductor Nanocrystals

Semiconductor nanocrystals, or quantum dots, are crystalline semiconductors on a size scale from $1 - 10$ nm, containing between 100 and 10,000 atoms. They are currently a subject of extensive research activity targeting a wide range of potential applications, including solid-state lighting,[4;5] photovoltaics,[6–8] and fluorescent tags for biological imaging.[9–11] Interest in nanocrystals is due to their unique size-dependent optical and electronic properties, chiefly a size-tunable optical absorption and emission spectrum.

In a bulk semiconductor, absorption of a photon by an interband transition typically generates a delocalized electron and hole within the system. A second possibility is the generation of a bound electron-hole quasiparticle state, known as a Wannier-Mott exciton. The electron-hole pair is weakly bound by a mutual Coulomb interaction and can be considered as a hydrogenic system with the electron and hole in a stable orbit. In a Wannier-Mott exciton, the electron and hole are spatially delocalized over several atoms and can move freely through the crystal.[12] In all semiconductors, the electron and hole will maintain a characteristic separation, known as the bulk Bohr radius. For CdSe, the nanocrystal used in this work, the bulk Bohr radius is 5.4 nm.

Size-dependent effects in nanocrystals are due to quantum confinement of free charge carriers. Confinement is defined as a spatial dimension reduced below the exciton radius. In this case the charge carriers can no longer move freely in this
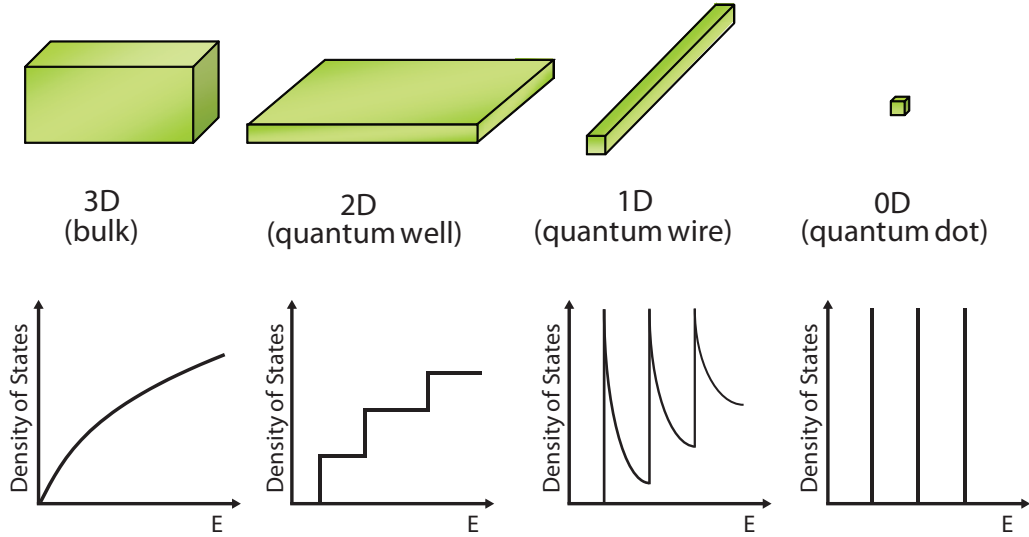
Figure 1.1: Quantum Confinement. From left to right, increasing degrees of confinement and the effect on the density of electronic states.

dimension. The most pronounced effect of confinement is on the density of states of the system. Figure 1.1 illustrates increasing degrees of confinement, beginning with bulk material. In order of decreasing dimension, there is the quantum well, the quantum wire, and finally the quantum dot. The quantum dot is a 0-dimensional system; free charge carriers are confined in all three spatial dimensions. At this point, the properties of the nanocrystal become strongly size dependent and the electron-hole pair can occupy only discrete energy states. In this sense, nanocrystals can be considered "artificial atoms."[13] Nanocrystals of various sizes, and their associated absorption spectra, are depicted in Figure 1.2.

1.3 Photovoltaics

1.3.1 Traditional Photovoltaics

The photovoltaic response of a traditional silicon solar cell is due to a *pn*-junction. When *n*-type silicon, typically doped with phosphorus, is diffused into *p*-type silicon, typically doped with boron, a planar interface is formed between the
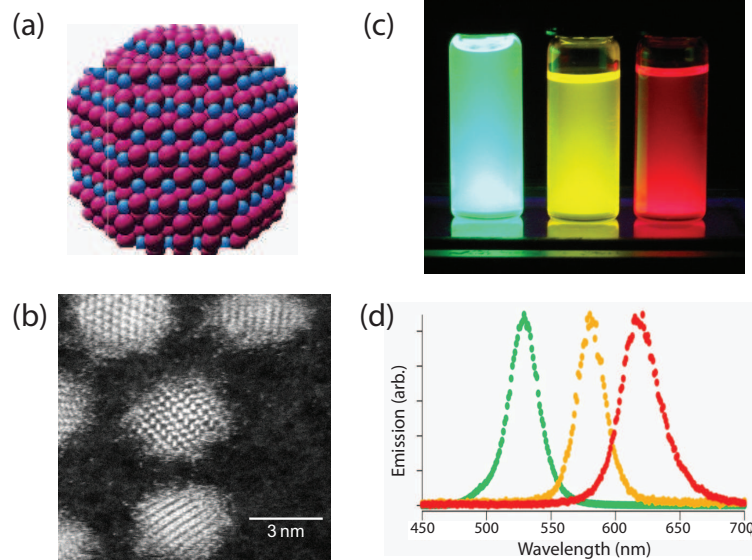
Figure 1.2: Semiconductor Nanocrystals. (a) Illustration of a CdSe nanocrystal. (b) STEM image of a CdSe nanocrystal. Note the clear fringe patterns, used to determine crystal structure. (c) Photograph of a range of nanocrystal sizes, and (d) their associated emission spectra, showing primary emission features in the visible.

two regions. Excess electrons in the n-region, driven by a difference in chemical potential, diffuse across the interface, combining with excess holes in the p-region, resulting in a net positive charge in the n-region, and a net negative charge in the p-region. A potential difference is established across the two sides, opposing further diffusion of majority carriers. This region is called the depletion region, reflecting the depletion of excess carriers. When a photon is absorbed inside this region, the generated electron-hole pair is separated by the force of the electric field. Once separated, the free carriers drift through the material and are collected at an electrode, yielding a DC photocurrent through an external path that can be used to power a load. A representation of the pn-junction as employed in a silicon photovoltaic is provided in Figure 1.3.

The silicon solar cell has two major sources of efficiency loss: (1) Carrier recombination in the bulk material, and (2) thermal losses. First, free charge carriers generated outside the photoactive region immediately recombine in the material, and
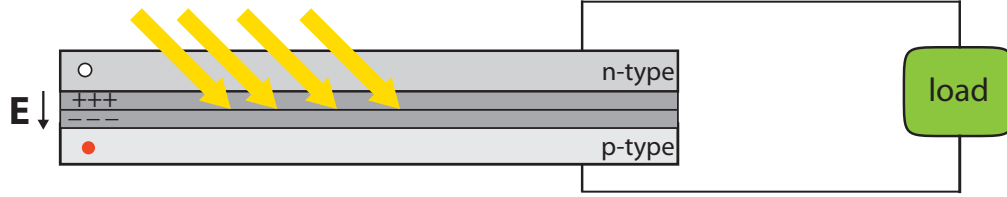
Figure 1.3: A silicon photovoltaic. Photons absorbed in the depletion region of the *pn*-junction can be separated and used to power a DC load.

do not contribute to the photocurrent. Even when free carriers are generated in the depletion region, there is still a possibility of recombination with minority carriers in the bulk material, present from defects and other impurities. The thicker the layer is, the higher the probability of recombination. Second, when a photon is absorbed, only one exciton is generated. Any energy in excess of the band gap energy is lost as heat. Thus the conversion efficiency of a *pn*-junction solar cell is band gap dependent. Stacking multiple semiconductor layers with different band gaps is a means of increasing the total fraction of the solar spectrum absorbed. Thermodynamic considerations have placed an ideal limit of 29% on single-layer silicon photovoltaics ($E_g = 1.1\,\text{eV}$), and 68% for a theoretical infinite layer device. These limits establish the well-known *Shockley-Queissar limit*.[14] While it is theoretically possible to generate an exciton for each multiple of the band gap energy through a process known as impact ionization, in bulk material this process is exceedingly inefficient.[15] This effect may be more efficient in nanocrystal systems, as discussed in more detail below.

Significant limitations exist on the performance of traditional photovoltaics, and to enable widespread deployment new paradigms are needed. Numerous alternatives to the traditional silicon photovoltaic design have been proposed, including *pn*-heterojunction, thin film, and organic polymer architectures. The use of nanostructured materials presents a compelling alternative. Our ability to engineer structures at the nanoscale provides us with the ability to fine tune the properties necessary for improved performance. A number of properties of nanocrystals make them an ideal

candidate for a novel photovoltaic device.

1.3.2 Nanostructured Photovoltaics

One of the more promising alternatives to silicon photovoltaic technology is the dye-sensitized solar cell (DSSC), also known as the Grätzel cell after its inventor.[16] The original Grätzel cell design is an electrochemical cell consisting of a matrix of porous, nanocrystalline TiO_2 deposited on the surface of a transparent conducting oxide (TCO). The TiO_2 nanoparticles are sensitized with an organic dye, typically Ru-based, and the matrix is infiltrated with a redox-coupling electrolyte. The photoactive dye molecules generate electron-hole pairs upon absorption of light, and the electron is transported to the TiO_2, where it is collected at an electrode and used to power a load. Donation of an electron from a redox couple in the electrolyte returns the dye to its ground state.

Power conversion efficiencies of the Grätzel cell have exceeded 10%, making the Grätzel cell competitive with existing commercial technologies. The high efficiency of this design is due to two features: (1) an increased photoactive region due to the porous TiO_2 surface; and (2) the separation of charge generation from charge transport, reducing carrier recombination of photogenerated charges. By immediately transporting the electron into the TiO_2, the chance for it to recombine with the generated hole is minimized. The low charge recombination rate has led to internal photon-to-electron conversion efficiencies greater than 80%. However, widespread deployment has been hindered by stability problems stemming from leakage of the liquid electrolyte and degradation of the organic light-harvesting dye, limiting the useful lifespan of the system. To avoid this difficulty, all solid-state designs have been proposed, for example organic, flexible polymer layers. However, current conversion efficiencies for these devices remain low.[17]

A number of studies have demonstrated that nanocrystals can be effectively

sensitized onto the surface of TiO_2, leading to the suggestion that they may be used as a light harvesting element, in place of the organic dye.[6;8;18]

The solar cell architecture reported in this thesis builds on the Grätzel cell design in three key areas:

1. CdSe nanocrystals as light harvesting element. Compared to organic dyes, inorganic semiconductor nanocrystals are more robust. The tunable band properties ensure optimzed absorption over the solar spectrum.

2. A highly-ordered TiO_2 nanotube array electrode, replacing the disordered matrix of TiO_2 nanoparticles. This structure has been shown to have favorable electron transport and mobility properties compared to nanocrystalline TiO_2, primarily because electron transport becomes inherently one-dimensional, compared to the percolation of electrons in a particle matrix.[19]

3. An all solid-state design employing solution-processed polymers for hole transport. One of the significant limitations of the original Grätzel cell design is the use of a liquid electrolyte redox couple, which is inherently unstable and prone to degradation and leakage. We circumvent this problem by using solid-state solution-processed polymers.

A diagram of the device structure is provided in Figure 1.4. The device is an ordered-heterojunction, solid-state, quantum dot-sensitized photovoltaic. The nanocrystals are chemically self-assembled onto the inner surface of the TiO_2 nanotubes using a bifunctional linking molecule, mercaptopropionic acid (MPA) (HOOC-CH_2-CH_2-SH). The nanotube pores are filled with transparent, hole-conducting polymers. A layer of N,N-bis(3-methylphenyl)-N,N-diphenyl-1,1?-biphenyl-4,4-diamine (TPD), followed by a layer of Poly(3,4-ethylenedioxythiophene) poly(styrenesulfonate) (PEDOT:PSS) are deposited by spin-casting. Precise alignment of the energy bands of adjacent layers ensures unidirectional charge transfer, as seen in Figure 1.5.
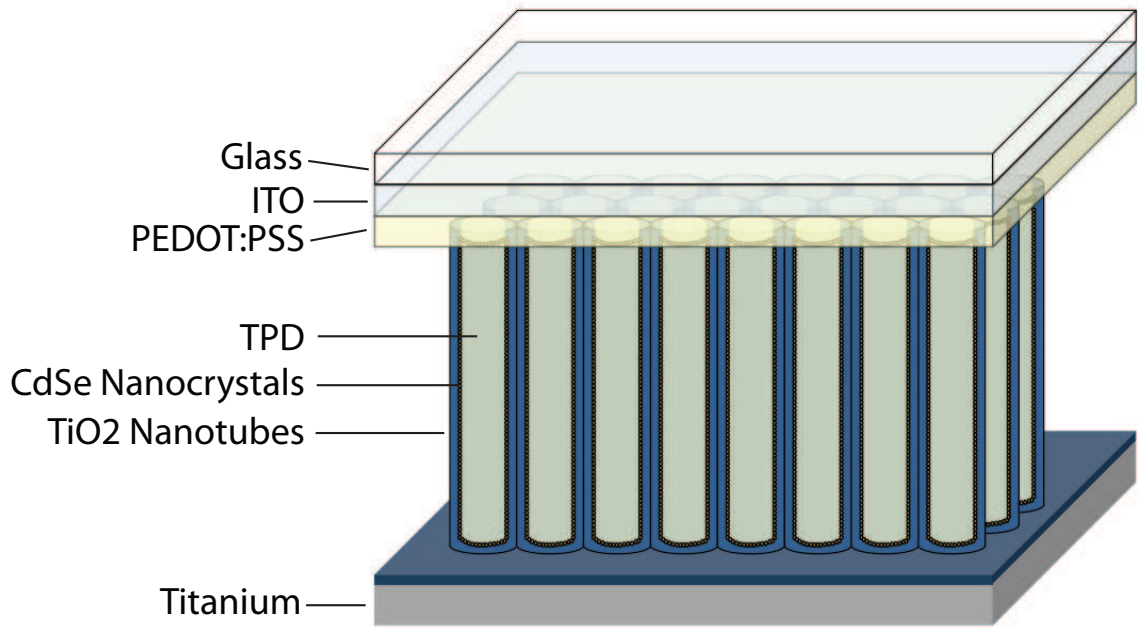
Figure 1.4: Cartoon of the experimental device structure.
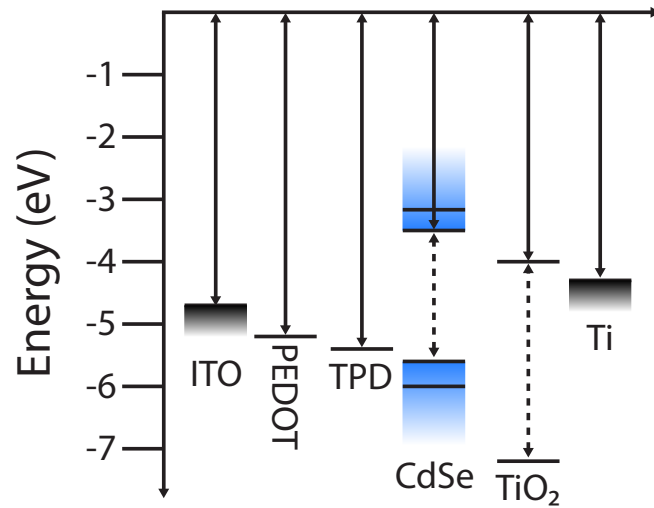
Figure 1.5: Energy band diagram of device layers. Precise alignment of the various energy bands ensures carrier separation and unidirectional charge transfer.

Nanocrystals offer a number of advantages over organic dyes. First, they are inorganic and highly robust. Second, their larger size acts to form a barrier between the TiO_2 electron conducting layer, and the ITO hole conducting layer, minimizing charge recombination. Third, they absorb a broader portion of the solar spectrum than dye molecules.[6] Because CdSe is the most well understood nanocrystal system, it has been used in our current device designs. Future devices may implement PbSe nanocrystals, as PbSe absorbs an even broader range of the solar spectrum (see Figure 1.6). Further information on PbSe can be found in Appendix A. Finally, nanocrystals have garnered significant excitement from recent reports of multiple exciton generation (MEG), a process by which more than one free electron can be generated per incident photon. Schaller *et al.* demonstrated the generation of seven exciton pairs from a single photon.[15] Exploiting this effect in a photovoltaic device could push the internal photon conversion efficiency (IPCE) beyond unity, making possible device efficiencies beyond current thermodynamic limits. To date, only one paper has reported an increase in internal gain attributed to MEG in a nanocrystal-based device.[20]

1.4 Nanostructured TiO_2 Films

The first phase of this research project centered on the fabrication of highly-ordered, nanostructured TiO_2 thin films to serve as the electron conducting layer in a nanocrystal solar cell. Building on earlier work in the group using an alumina-template embossing method, an alternative approach employing the electrochemical anodization of titanium thin films was developed. This method was successfully employed to fabricate large-area arrays of high quality, vertically-oriented TiO_2 nanotubes.
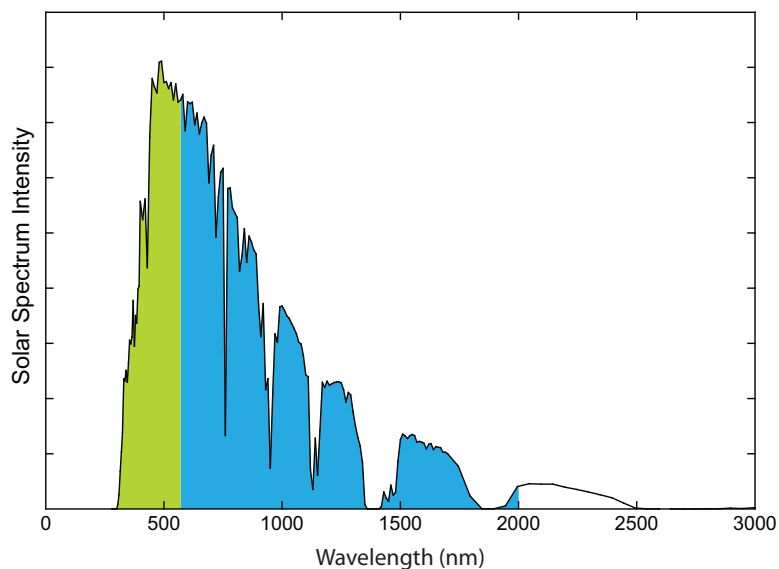
Figure 1.6: Solar spectrum coverage of CdSe and PbSe nanocrystals. Green is CdSe absorption and blue is PbSe absorption.

1.4.1 Nanocrystalline TiO$_2$ Films

The efficiency of a dye-sensitized photovoltaic depends on the number of dye molecules absorbed onto the surface of the TiO$_2$ electrode. Hence, one practical way of improving device efficiency is to increase the total surface area available for sensitizing. In his initial device, Grätzel utilized a matrix of TiO$_2$ nanoparticles deposited via doctor blading. The porous film has a much larger surface area available for sensitizing than a planar film.

1.4.2 Ordered Nanostructured TiO$_2$ Films

Charge collection in a porous nanocrystalline TiO$_2$ electrode depends on carrier hopping through the TiO$_2$ matrix, generally described in terms of a percolation process.[17] Charge hopping increases the chance of carrier recombination across crystal boundaries and defect sites. An important improvement would be the utilization of an *ordered* nanostructured TiO$_2$ thin film, which would decrease the chances of carrier recombination by shuttling electrons through a one-dimensional electrode.
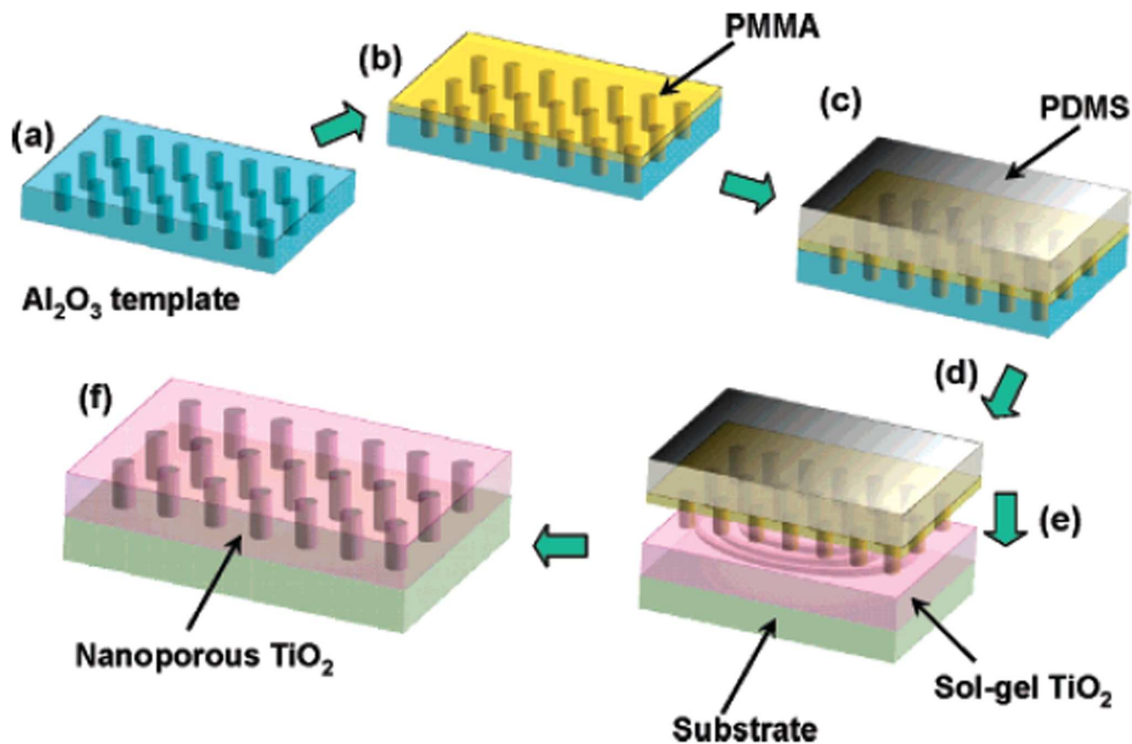
Figure 1.7: Alumina Templating Procedure. Adapted from Goh *et al.*[21]

Previous Work: Alumina-Template Embossing

Previous work in the Rosenthal lab directed at fabricating structured TiO_2 layers focused on an alumina-template embossing procedure developed by Goh *at al.*[21] The procedure is outlined in Figure 1.7. Poly-(methyl methacrylate) (PMMA) is drop cast onto an alumina template with a 50 nm pore diameter. The sample is heated to 200 °C to infuse the polymer into the pores. A backing layer of poly(dimethylsiloxane) (PDMS) is coated onto the PMMA layer and allowed to cure at room temperature. A wet chemical etch separates the polymer layer from the alumina foil. A thin film of sol-gel TiO_2 is then spin-cast onto an ITO-coated glass slide. Immediately after spin-casting, the polymer layer is pressed onto the TiO_2 film, embossing pores into the film. The polymer layer is removed, and the sample is annealed to crystallize. SEM characterization of embossed TiO_2 sol-gel is provided in Figure 1.8.

11
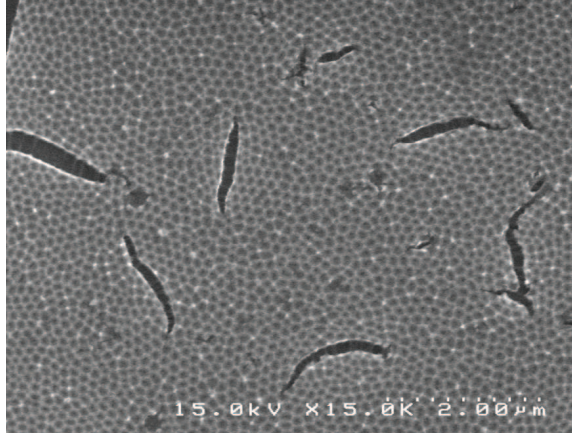
Figure 1.8: Alumina Templating SEM Image

While this method is capable of producing pores of uniform diameter with consistent distribution, it suffers from a number of significant drawbacks. First, the technique is difficult and requires several intermediate steps before a titania sample is fabricated. The polymer intermediary is highly prone to damage. Second, the surface coverage of pores on the TiO_2 film is poor. The creation of pores is a result of embossing by the polymer layer, and differences in applied pressure can drastically affect the resulting film quality. Third, the technique scales inefficiently and is limited by the size of the alumina template. The largest surface coverage acheived using this method has been $\sim 0.25\,cm^2$. Fourth, maximum pore depths have been on the order of hundreds of nanometers, while other techniques have achieved micron-scale pore depths. Deeper pores are necessary to maximize the amount of nanocrystals loaded onto the electrode surface. These drawbacks pointed toward the need for an alternative method of fabricating a nanostructured TiO_2 electrode.

Potentiostatic Anodization of Titanium Films

Anodization of titanium in a fluorine-containing electrolyte has been shown to result in a vertically-oriented array of TiO_2 nanotubes. TiO_2 nanotubes formed in this way have been explored for a variety of applications, including water photo-

electrolysis, photocatalysis, and gas sensing.[22] For photovoltaic applications, the anodization method offers several advantages over alumina-template embossing. First, it is simpler. Formation of the self-assembled nanotube array is a single-step process. Second, the anodization results in uniform surface coverage. Third, control of the anodization parameters allows control of the resulting film morphology: tube length ($1\,\mu$m-$1000\,\mu$m), pore diameter ($75\,$nm-$150\,$nm), and wall thickness ($8\,$nm-$12\,$nm).[22] The parameters available for adjustment include anodization voltage, duration and electrolyte composition. Additionally, there appears to be no limit to the overall nanotube length. In 2007, Prakasam *et al.* used the method to form a self-standing, $720\,\mu$m thick TiO_2 nanotube layer, starting with a titanium foil only $250\,\mu$m thick![23] Prakasam attributed this result to a nearly complete conversion of Ti to TiO_2, in which excess etched titanium in solution binds with free oxygen in the electrolyte, forming TiO_2, and subsequently moves under influence of the electric field towards the nanotube-solution interface. The free TiO_2 molecules then bind to the top ends of the nanotubes. In this way, nanotube growth proceeds not only downwards through the titanium layer, but upwards as additional TiO_2 is added onto the top end of the nanotubes.

CHAPTER II

EXPERIMENTAL

2.1 Introduction

This chapter details the experimental procedures utilized during this project. Section 2.2 covers the protocol for CdSe nanocrystal synthesis and isolation. Section 2.3 describes the preparation of anodized TiO_2 nanotube arrays from titanium foils and titanium thin films. Section 2.4 describes three techniques of nanocrystal deposition: drop cast and immersion, chemical linking, and electrophoretic deposition (EPD). Section 2.5 describes the integration of the consituent components into a working photovoltaic device. Finally, Section 2.6 describes methods of imaging and characterization employed throughout the fabrication process.

2.2 Synthesis of CdSe Nanocrystals

Semiconductor nanocrystals were synthesized according to standard one-pot procedures, involving the high temperature pyrolysis of organometallic precursors and subsequent nucleation and growth of individual nanocrystals.[24] This colloidal, bottom-up synthesis is advantageous for its relative simplicity and the uniform size distribution of the resulting nanocrystals.

The pyrolysis method is outlined in Figure 2.1. First, the selenium complex is formed by dissolving 0.96 g Se powder (Aldrich, 99.999%) in 100 mL of tributylphosphine (TBP, Aldrich, 90%). Next, the cadmium complex is formed by mixing the following chemicals in a three-neck flask: 0.257 g cadmium oxide (CdO, Strem, 99.99%), 6.0 g trioctylphosphine oxide (TOPO, Aldrich, tech grade 90%+), 4.0 g hexadecyl amine (HDA, Aldrich, 90%), and 1.0 g dodecylphosphonic acid (DDPA, in-house syn-

thesis). The solution is heated under argon purge using a heating mantle to $150\,°C$, then brought to $330\,°C$ under passive argon. The solution is vigorously stirred until cadmium phosphonate is formed and the solution turns clear. Once clear, the temperature is reduced to $315\,°C$, and $10\,mL$ of the Se:TBP solution is injected into the flask, initiating nanocrystal nucleation and growth. The solution is held at $260\,°C$ for growth. Initial growth is rapid for the first few minutes, slowing down over the next twenty minutes. The nanocrystals are allowed to grow to the desired size, then removed from the heating mantle and cooled with compressed air to stop the growth process. To determine the nanocrystal size, a small amount of solution is pulled from the reaction vessel and diluted with toluene. An absorption spectrum is taken with a Cary 50 Bio UV-Visible Spectrophotometer, and the first major absorption feature is compared with standard literature values for a size estimate.[25]

Once the desired size is achieved, a cleanup procedure is performed to recover and isolate the nanocrystals. The pot solution is transferred to vials, diluted with methanol and centrifuged at 4500 rpm for three minutes to precipitate the nanocrystals. The liquid is discarded and the vial filled with $6\,mL$ octanol and centrifuged at 4500 rpm for 30 minutes. This cleanup process is repeated as many times as necessary, however nanocrystals are lost with each cycle. As synthesized, this preparation yields CdSe nanocrystals with surface cadmium atoms passivated by TOPO, HDA, and DDPA. The nanocrystals are stored in solution, typically dissolved in either hexanes or toluene. Pyrolytically synthesized CdSe nanocrystals with a first absorption feature at $580\,nm$, corresponding to an average size of $3.75\,nm$, and dissolved in hexanes, were used in these experiments. Future experiments should examine the role of nanocrystal size on device performance.
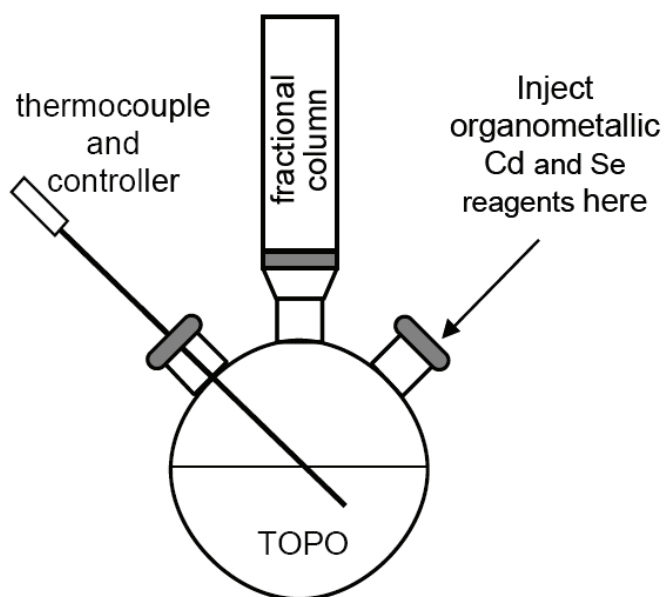
Figure 2.1: Standard nanocrystal synthesis configuration

2.3   Fabrication of Ordered TiO$_2$ Nanotube Arrays

Titanium foils, $250\,\mu$m thick, were obtained from Sigma-Aldrich and cut to $6.25\,cm^2$ using a machine shop press. Prior to anodization, the samples were degreased by sonicating in 2-propanol and acetone.

Anodizations were performed in a specially machined etch cell, depicted in Figure 2.2. The cell consists of a square Teflon base and bowl-shaped cell chamber. At the base of the cell chamber is a circular opening. A rubber O-ring is used to prevent electrolyte leakage. A titanium foil was placed directly beneath the opening. A thin piece of copper was used as a back electrode. A platinum wire, bent into a spiral, acts as an inert counter electrode. The wire is held in place by a brass support ring. The copper anode and platinum cathode were connected to a Kiethley 2400 source meter, interfaced with an Apple G3 running custom LabView software to monitor the anodization current. The anodization is started and stopped automatically in Lab-View. A screenshot of the Labview interface is provided in Figure 2.3. Anodization voltage and time, and ramp rates, can be user defined. To prevent contamination of the electrolye, the anodization is performed in a fume hood.

Electrolyte solutions contained either Potassium Fluoride (KF, Sigma-Aldrich, 99%) or Ammonium Fluoride (NH$_4$F, Sigma-Aldrich, 98%). Sonication and mild heating was typically required to dissolve the fluorine source into solution. Organic-based solutions used either ethylene glycol (Fischer, 99.8%) or formamide (Fischer, 99.8%) as a solvent.

After the anodization was completed, the sample was removed from the etch cell. The sample was rinsed in ethanol and deionized water, and dried under a nitrogen stream. A mild sonication in ethanol (under one minute) was necessary to clear surface debris.

As fabricated, the nanotubes are amorphous TiO$_2$. Device applications require the higher conductivity of anatase TiO$_2$. To crystallize into anatase TiO$_2$, a Lindberg-
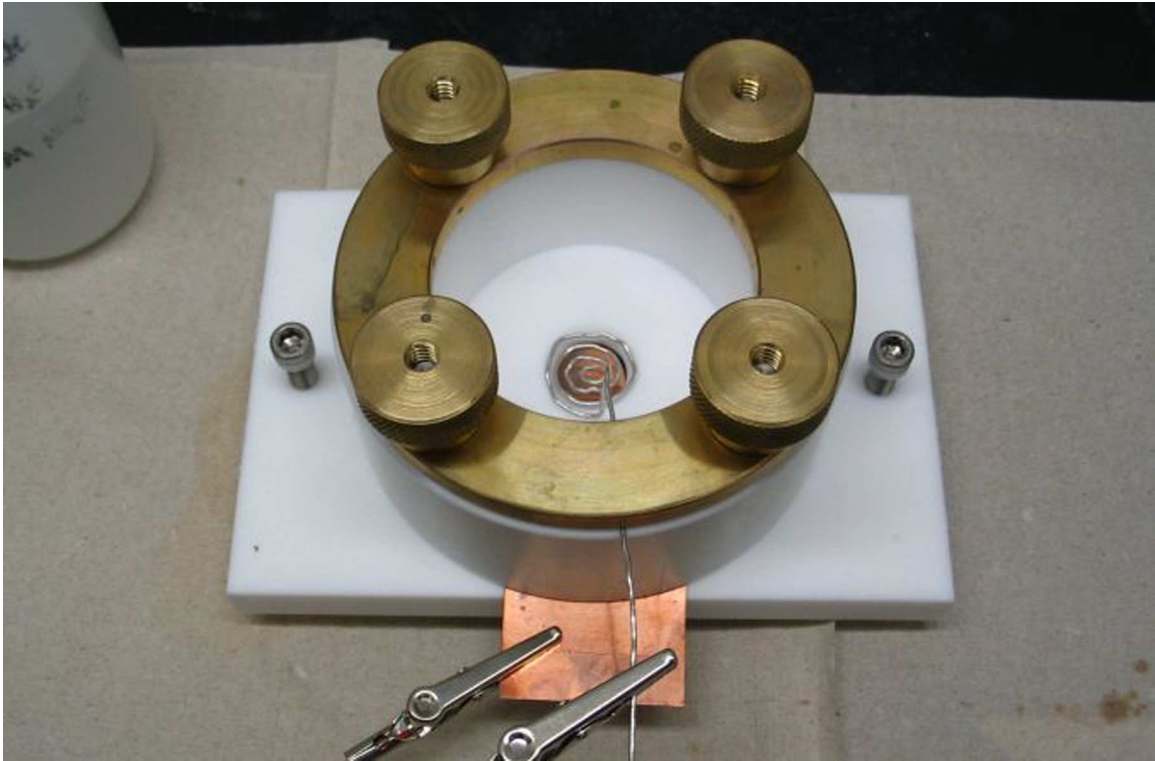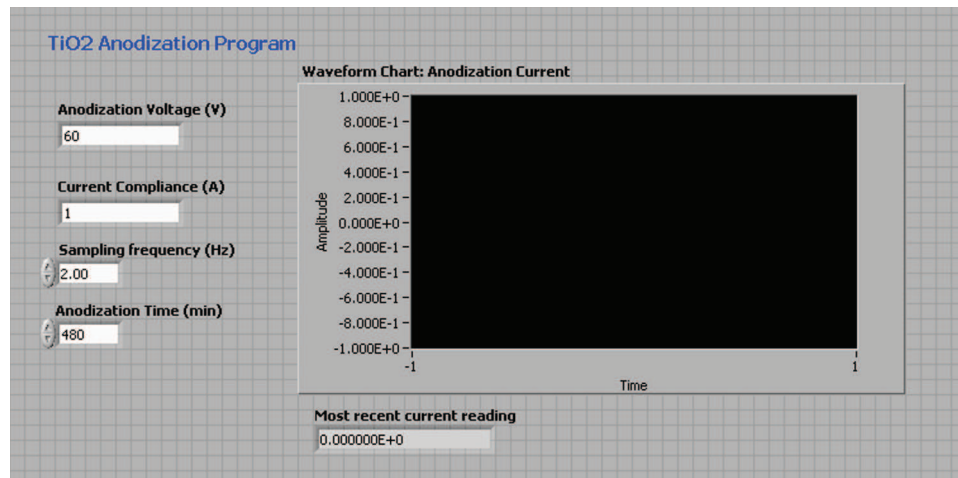
Figure 2.2: Anodization Setup

Figure 2.3: Screenshot of custom LabView interface controlling anodization.

Blue HTF55000 Series Hinged Tube Furnace with a quartz tube was used to anneal the samples at high temperature. Samples were annealed in atmosphere at 450 °C for 5 hours with ramp periods of 3 hours (2.5 °C/min).

2.3.1 Thin Film Anodization

The original technique of anodizing titanium foils suffers the drawback of having the nanotube arrays bound to an opaque titanium substrate. This limits possible device architectures to only those in which light is illuminated on top of the nanotube layer (backside illuminated). Earlier groups had reported that nanotubes could be successfully fabricated from a starting point of a thin film of titanium on the surface of a transparent conducting oxide.[26]

A thin film of titanium was deposited via electron-beam evaporation onto an ITO-coated glass slide. Films of thickness between 300 and 500 nanometers were deposited at a controlled rate of approximately 10 nm/min. The etch was carried out in an identical fashion to the foil etch, except that a small piece of aluminum foil was wrapped around the edge of slide to faciliate electrical contact at the anode.

Electron beam physical vapor deposition is a standard technique for deposition of metallic thin films. A high energy electron beam is aimed at a source target, which creates local heating and evaporation of the material. The evaporated material diffuses outward and precipates on the sample, forming a film. Control of the electron beam parameters will control the rate of evaporation and consequently the rate of deposition. Here, a high purity titanium target was used to deposit titanium thin films.

Because of the greatly reduced thickness of the titanium thin films, it was expected that the etch process would be complete much more rapidly than with the titanium foil. Experiments determined that within 10 minutes the etch was fully complete, compared to several hours for a typical foil etch. It appeared that the

entire titanium had been etched away and nothing remained, as the slide was transparent in the region, however SEM confirmed the presence of a unique microstructure of titanium. Attempts were then made to control the etch parameters, chiefly the anodization voltage and time. It was expected that a clear drop in current should be visible once the titanium layer had been completely etched away, however no such feature was observed. Attempts to control the fabrication to produce ordered arrays were unsucessful.

2.4   Nanocrystal Deposition

The second phase of the project was to sensitize the TiO_2 surface with CdSe nanocrystals. Three methods were attempted: drop cast and immersion, chemical linking, and electrophoretic deposition.

2.4.1   Drop Cast and Immersion

Two simple methods were tried to initially test nanocrystals deposition. First, a small amount of nanocrystal solution was drop cast onto the sample by pipette. Second, samples were allowed to sit immersed in a dilute nanocrystal solution for a period of time ranging from 6 to 48 hours. After each procedure, the sample was rinsed with toluene to remove unbound nanocrystals from the sample surface.

2.4.2   Chemical Linking

Chemical linking is a well established technique of using a bifunctional linker molecule (HOOC-R-SH) to attach CdSe and CdS nanocrystals to the surface of the TiO_2 substrate.[27] The TiO_2 is strongly attracted to the carboxylate group, while the thiol group binds strongly to the CdSe nanocrystal. An outline of the process is provided in Figure 2.4.

Mercaptopropionic Acid (MPA) (HOOC-CH_2-CH_2-SH) was used as a linker
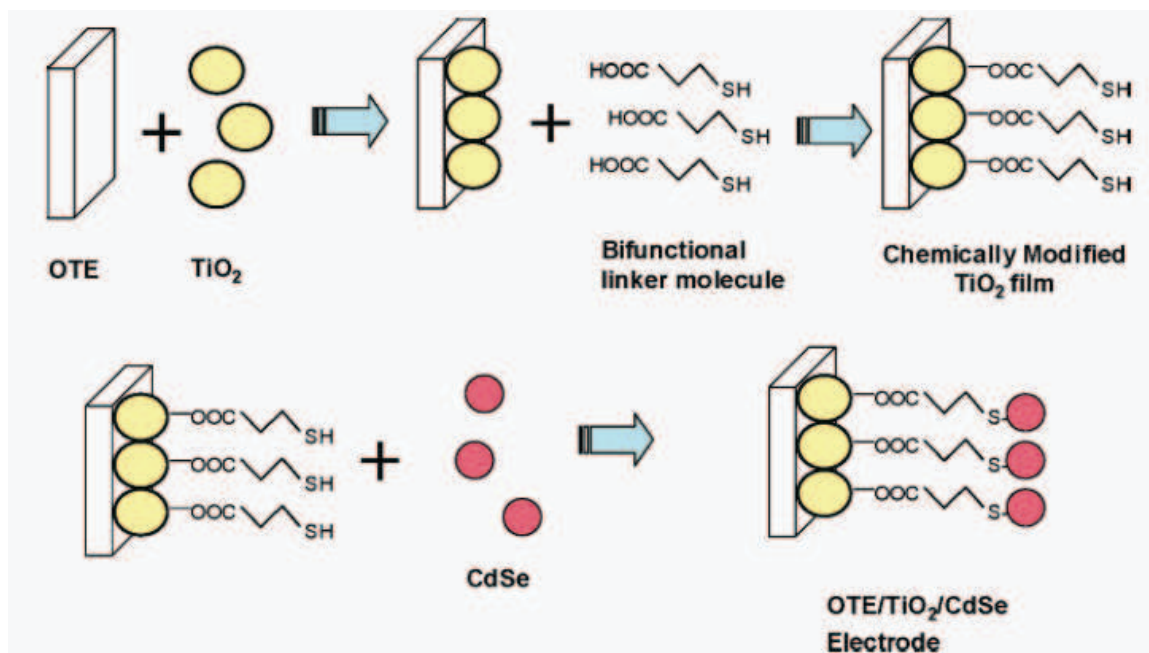
Figure 2.4: Chemical linking cartoon. The TiO$_2$ is functionalized with the MPA linking molecule and then immersed in a nanocrystal solution. Adapted from Robel et al.[27]

molecule to bind CdSe to the TiO$_2$ nanotube arrays. A solution of 10 vol% MPA in acetonitrile was prepared, following Robel et al.[27] Anodized TiO$_2$ samples were immersed in this solution between 4 and 24 hours. After immersion, the electrodes were rinsed thoroughly in acetonitrile to remove unbound MPA, and then immersed in dilute nanocrystal solutions of varying optical density for between 12 and 96 hrs. Finally, the samples were rinsed in toluene to remove unbound nanocrystals.

2.4.3 Electrophoretic Deposition

Electrophoretic Deposition (EPD) is a straightforward application of an electrochemical cell.[28] Two electrodes are immersed in a bath containing a dilute solution of nanocrystals in a non-polar solvent. At room temperature, some of the nanocrystals will be thermally charged. When a voltage is applied between the two electrodes, the nanocrystals migrate under the influence of the electric field towards either elec-
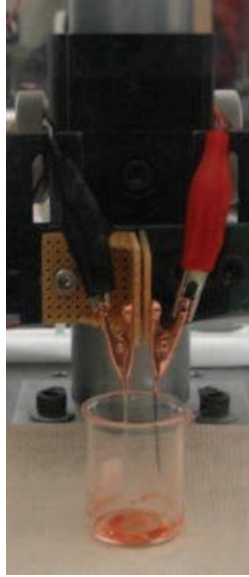
Figure 2.5: Electrophoretic Deposition (EPD) experimental setup. Containing the apparatus within a plastic casing allows the composition of deposition environment to be controlled. Specifically, a nitrogen purge is used to reduce the atmospheric humidity.

trode. Once they reach the electrode, the nanocrystals become bound to the surface, most likely through Van der Walls attraction. The experimental setup is depicted in Figure 2.5. In this setup, an ITO slide acts as one electrode, while the TiO_2 nanotube array acts as the opposite electrode. Results have indicated that deposition will occur on electrodes of either polarity.[7]

CdSe nanocrystals, dissolved in hexanes, were deposited onto TiO_2 nanotube arrays under a driving potential of 500 Volts and separation distance of 1 cm. The experiment was run under a nitrogen atmosphere to minimize evaporation of the solvent. Standard deposition time was 15 minutes. After completing the deposition, the electrodes were removed from solution and held in air for 5 minutes, allowing the nanocrystal film to anneal.

2.5 Device Fabrication

2.5.1 ITO Patterning

To reduce the possibilty of defects in the device and increase the total sample size, the active area of each device was reduced by selectively patterning the ITO slide through an HCl etch. The active area of each device was then taken as the overlap between the ITO coated region and the TiO_2 sample. Etching the ITO was accomplished by using $4\,M$ HCl heated to $60\,°C$ in a water bath under constant stirring. Patterning was achieved by selective masking with electrical tape. After immersion for 15 minutes, the unmasked regions of ITO were fully etched away, with a sharp interface between the ITO and etched regions. Following the etch, the tape was removed and the sample sonicated in acetone and 2-propanol to remove any excess tape residue.

For the devices reported in this thesis, the ITO was etched in a pattern that allowed six samples to be fabricated per ITO slide. Each section was approximately $2\,mm$ wide by $6\,mm$ long.

2.5.2 Polymer Deposition

Hole-conducting polymer layers form a heterojunction interface to promote efficient charge separation off of the nanocrystal. Solution-processable polymers were chosen for their ease of use and deposited by spin-casting. A TPD solution of $10\,mg$ TPD per $1\,mL$ chloroform was made and deposited onto the nanotube sample by spin-casting at $1000\,RPM$ for $60\,s$. A solution of PEDOT:PSS was then diluted 50:50 in water and deposited onto the sample by spin-casting at $2000\,RPM$ for $60\,s$. The sample was annealed at $100\,°C$ for $30\,minutes$ to cure, followed by $5\,minutes$ at $175\,°C$ to help drive the polymer into the pores.[29]

2.5.3 *Photovoltaic Device*

A thin film of PEDOT:PSS was spun-cast onto the patterned ITO slide. The ITO slide was then baked for 30 minutes at 100 °C to anneal the PEDOT:PSS layer.

The prepared TiO_2 layer was cut using the machine shop press to allow an ITO contact onto the sample without contacting a titanium layer (a drawback to anodization on titanium foil). The edge often proved to be a source of shorts, and was insulated using a very thin strip of fingernail polish. The device was finalized by sandwich-pressing the Ti foil and ITO slides, mediated by the PEDOT:PSS intermediate layer. The sandwich construction was held in place using binder clips, or when assembled into the home-built device tester.

2.6 Imaging and Characterization

Several instruments were used to characterize the nanotube films. For measurements of pore diameter and wall thickness, as well as analysis of film quality, a Hitachi S-4200 Scanning Electron Microscope (SEM) was used. This has recently been superseded by a Raith eLINE SEM, which is capable of imaging at a much higher resolution. Data using this device was not available while writing this thesis. An SEM works by collecting the secondary electrons scattered when a sample is exposed to a high-energy electron beam (15 keV). Generally, an SEM is best at imaging features on a scale 10-1000 nm, and thus proved very useful for imaging nanotube arrays with features on the order of 100 nm. Samples could be directly imaged without destructive preparation procedures, allowing the progress of a single sample to be tracked as the stages of device fabrication were completed.

Higher resolution images, as well as crystallographic and composition information, was obtained using a Philips CM20 Transmission Electron Microscope (TEM). The principle of TEM is the detection of electrons transmitted through a specimen

when subject to a high-energy electron beam (200 keV). TEM was used to characterize nanotube quality and verify nanocrystal deposition. For the purposes of this project, the resolving power of the TEM was generally more than necessary for basic characterization.

Higher resolution images, crystallographic information, and elemental composition were obtained using a Philips CM 20T Transmission Electron Microscope (TEM). TEM data was collected with the assistance of Dr. James McBride.

Two complementary methods were used to measure nanotube length. One was the mechanical fracturing of the sample prior to SEM imaging. Fracturing dislodged planes of the array and allowed a profile view of the layer to be imaged. From this, the approximate nanotube length could be determined. The second method was to remove the nanotube layer entirely, generally by scraping away the layer. A Veeco Dektak profilometer was then used to measure the step height difference between the anodized and unanodized section of titanium foil.

Elemental composition, important for verifying nanocrystal deposition, was determined using Rutherford Backscattering Spectroscopy (RBS) and Energy Dispersive X-Ray Spectroscopy (EDS). RBS is a technique whereby high energy alpha particles are incident on a sample surface. Analysis of the energy of backscattered ions can be used for elemental analysis. Vanderbilt operates a $1.8\,\mathrm{MeV}$ van de Graaff accelerator outfitted for RBS analysis. EDS is an extension of SEM functionality. A high-energy electron beam is incident on a substrate, exciting atoms on the surface. X-rays emitted from the relaxation of these atoms can be measured to obtain a unique signature of the elements present in the sample.

Note: Imaging Within Nanotubes

A word on imaging the nanotube-nanocrystal composite structure. The system has proven difficult to image for a number of reasons. One, the mass contrast difference between TiO_2 and CdSe makes it difficult to pick out the CdSe nanocrys-
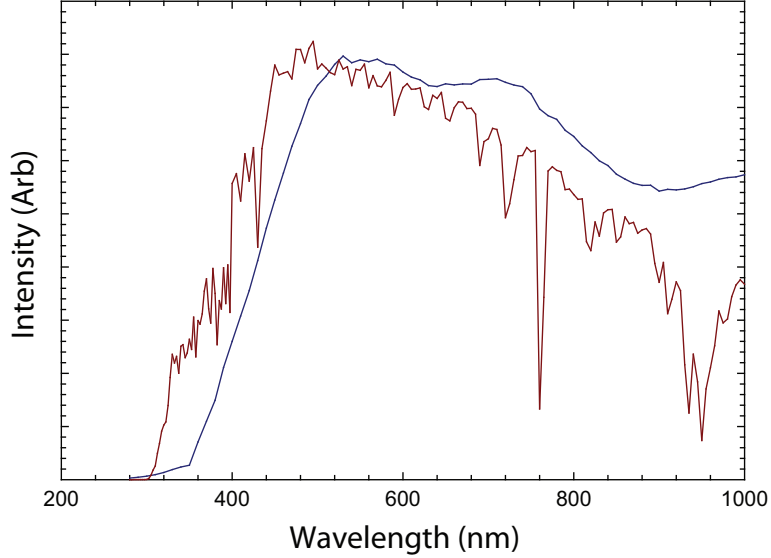
Figure 2.6: Spectral profile of Solux 4700K lamp used for device characterization. Red is solar spectrum and blue is the test lamp spectrum.

tals. Two, when the CdSe is attached to anatase-TiO_2 nanotubes, the fringe patterns overlap and prove difficult to identify. One solution to this was to skip the anneal stage of the anodization, and link nanocrystals to amorphous TiO_2 samples. This proved to be a helpful technique, if only for imaging purposes. Three, it is difficult to get a sense of the uniformity of coverage in the TEM. Nanocrystals bound to the nanotube surface can be seen only in profile, with no indication of the depth of coverage.

2.6.1 Device Characterization

Completed devices were characterized under solar-spectrum illumination from a 50 W Solux 4700K lamp with an average incident power intensity of $10\,mW/cm^2$ at room temperature in atmosphere. The spectral profile of the Solux lamp mapped against the solar spectrum at the Earth's surface is given in Figure 2.6.

Testing was performed in a home–built solar testing station consisting of a steel box painted black on the interior surface, with an coverable entrance slit. The
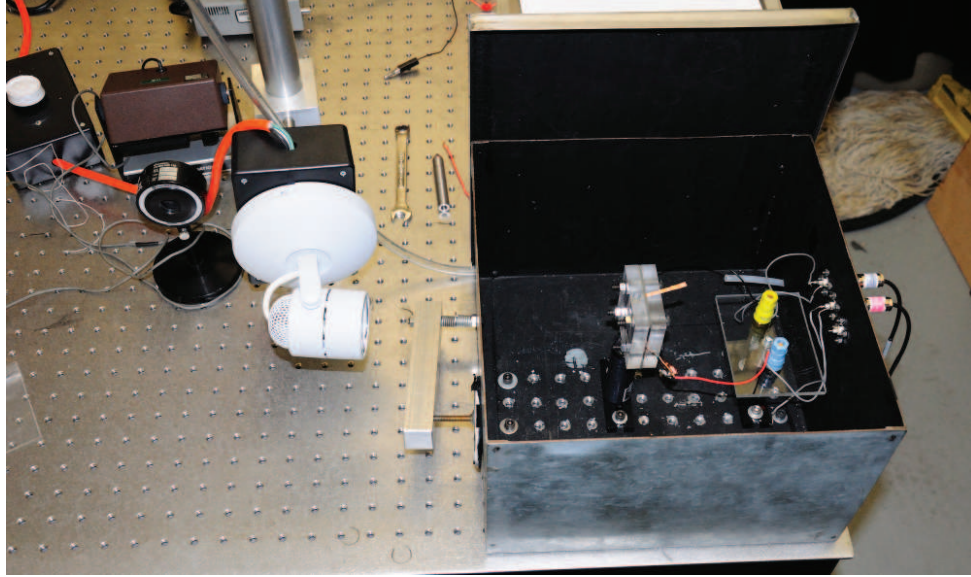
Figure 2.7: Solar Testing Station.

solar lamp was placed approximately 25 cm from the surface of the device. A photograph of the testing station is shown in Figure 2.7. Initially, a focusing lens and iris aperature was placed in the light path to concentrate light on the surface of the device, however it was later decided that the inhomogeneous spectral distribution of the focused light would make it more difficult to measure the average incident power intensity illuminating the device. A Coherent Radiation Model 210 Power Meter was used to measure incident power intensity.

CHAPTER III

FABRICATION AND CHARACTERIZATION OF HIGHLY-ORDERED TIO$_2$ NANOTUBE ARRAYS

3.1 Introduction

This chapter details the fabrication of highly-ordered TiO$_2$ nanotube arrays via the anodic oxidation of titanium foils. These ordered nanotube films act as the electron transport layer in the nanocrystal-sensitized photovoltaic described in this thesis. Section 3.2 discusses the fabrication of the TiO$_2$ nanotube array and summarizes the major experimental results. Section 3.3 provides discussion of these results and includes a description of the anodization mechanics. Finally, Section 3.4 discusses a technique of growing transparent films of TiO$_2$ nanotubes on a conducting glass substrate.

3.2 Results

3.2.1 General Nanotube Morphology

Anodization of titanium foil in a fluorine-ion containing electrolyte leads to the self-assembled formation of a highly-ordered nanotube array. SEM images of a characteristic sample at several magnifications are provided in Figure 3.1, showing highly-ordered nanotubes with clearly defined walls and long-range order. The pore diameters are $\sim 140\,\text{nm}$ and the wall thicknesses are $\sim 10\,\text{nm}$. Figure 3.2 shows TEM images of a portion of a similar nanotube sample in both plan and profile views.

Surface coverage is greatly improved compared with the alumina templating technique. Figure 3.3 compares the final result of the two techniques. The anodization technique creates a uniform film entirely over the surface of the foil, limited only by
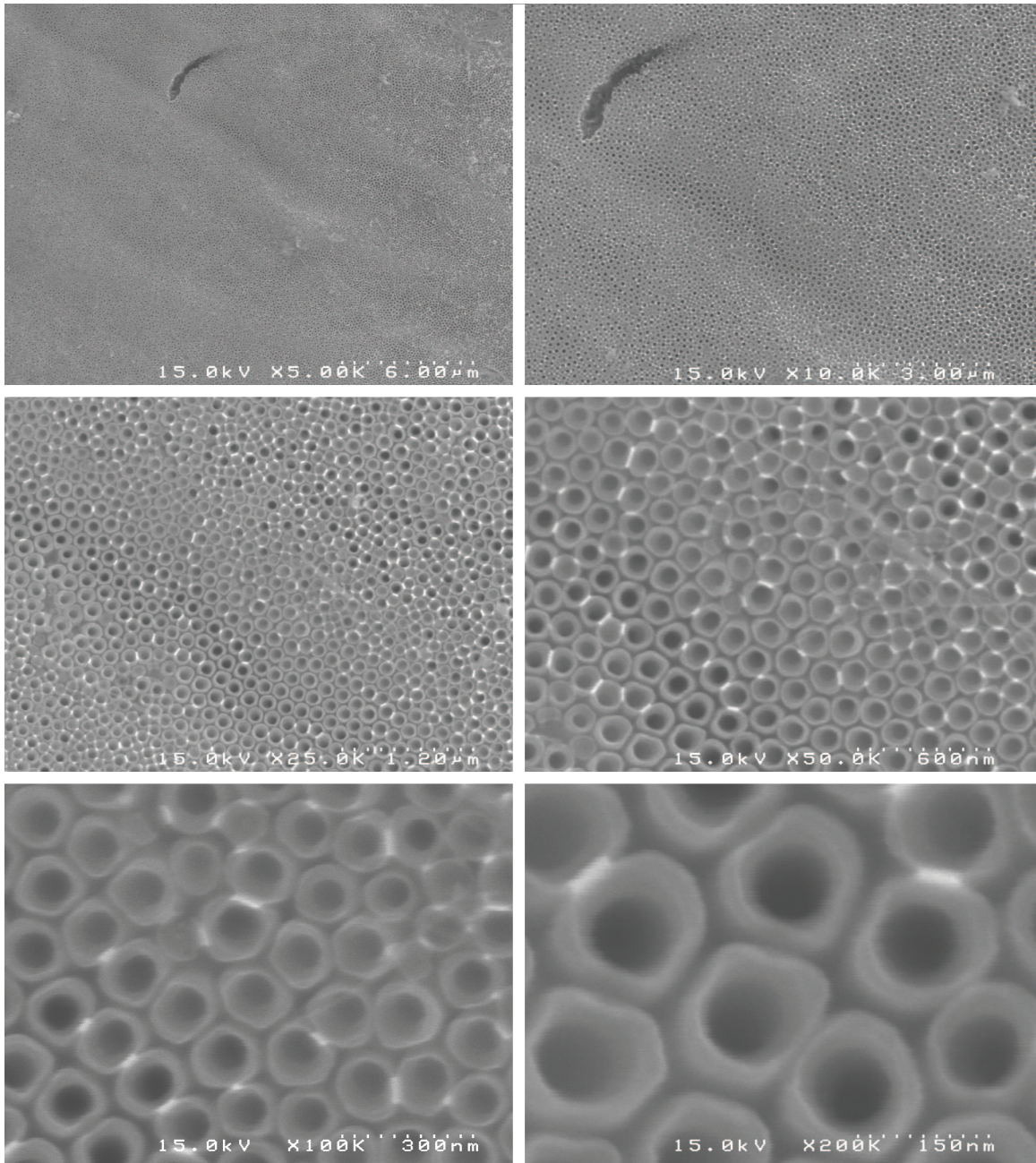
Figure 3.1: SEM series of a single TiO$_2$ nanotube array sample showing long-range order and discrete nanotube structure.
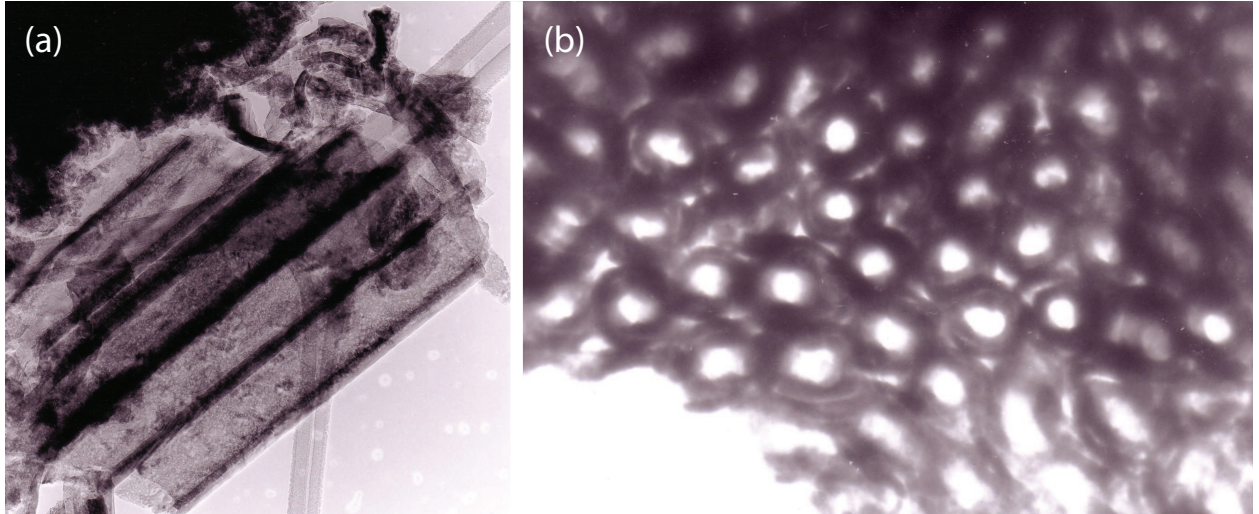
Figure 3.2: TEM of TiO$_2$ nanotubes. (a) Profile view. (b) Plan view

the area in contact with the electrolyte.

Nanotube morphology can be controlled by varying anodization parameters. Nanotube length depends primarily anodization duration. Pore diameter and wall thickness depend on both anodization voltage and electrolyte solution. The electrolyte composition was found to have the strongest effect on nanotube formation. Anodization voltage must then be chosen within a narrow range to allow for nanotube growth.

3.2.2   Effect of Electrolyte on Nanotube Morphology

Anodizations were performed using both aqueous and organic electrolytes. Aqueous electrolytes have the advantage of requiring a lower anodization voltage and less time, however the quality of the resulting nanotube array is poorer than that of an organic electrolyte. The standard aqueous electrolyte consisted of 0.1 mol KF and 1.0 mol H$_2$SO$_4$ in water.

Organic electrolytes proved to be more robust and allow for longer nanotube growth than the aqueous electrolytes. The standard organic electrolyte consisted of
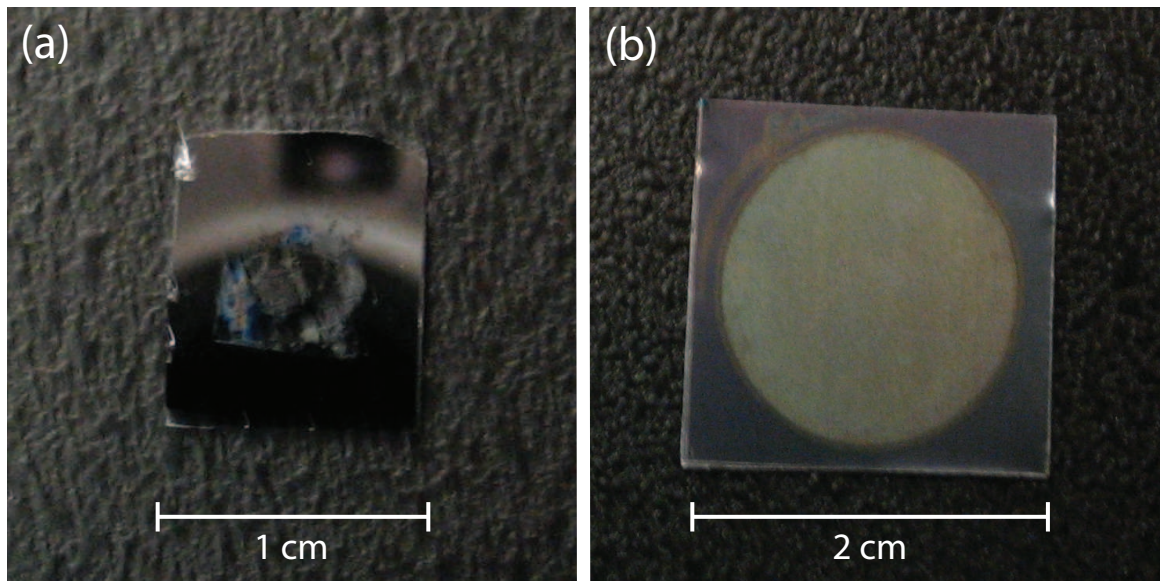
Figure 3.3: Comparison of (a) template and (b) anodization techniques. Anodization is completely scalable with uniform features of the surface of the sample. Templating works selectively other a smaller area and is limited in scalalbility.

0.25 wt% NH_4F in ethylene glycol. The viscosity of the organic electrolyte acts to counter the motion of the fluorine ions in solution, slowing the etch process down. Hence organic etches require much longer amounts of time; however this yields nanotube films of much more uniform quality. Specifically, etches in aqueous electrolytes could be completed in about an hour, while an etch of equivalent length in an organic electrolyte could require between eight to ten hours.

Figure 3.4 provides SEM images contrasting the nanotube morphology when anodized in aqueous and organic electrolytes. The organic electrolyte results in a nanotube array that is more tightly packed and has a more uniform and consistent morphology, compared with the aqueous electrolyte, which results in a nanotube array that is less ordered and more prone to surface damage at the nanotube tips.

Table 3.1 summarizes the electrolytes used in this study, and corresponding voltage ranges for which nanotube formation was observed. (For the formamide
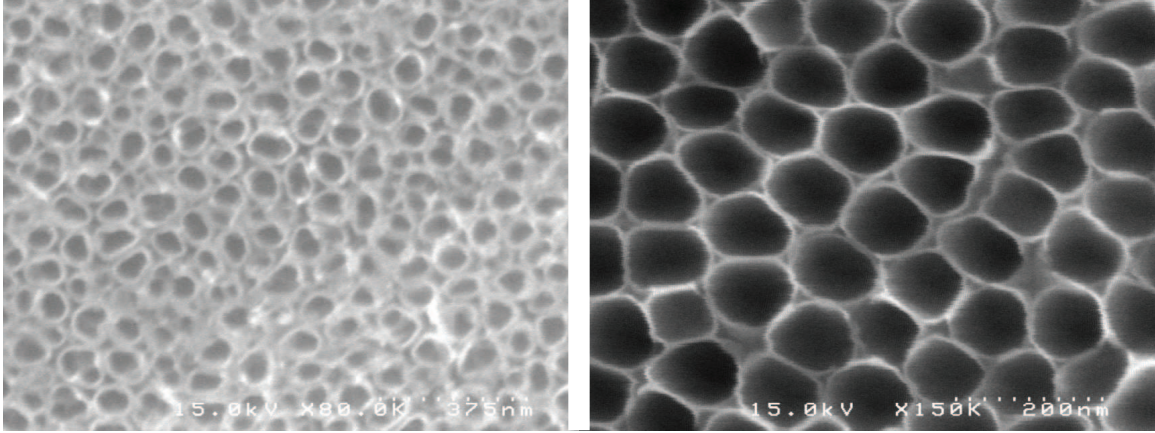
Figure 3.4: A comparison of aqueous and organic electrolyte anodization environments. The left panel was anodized in a 0.1 mol KF solution for 1 hour at 15 V, the right panel in 0.25 wt% NH$_4$F in Ethylene Glycol for 14 hours at 60 V. Clearly visible is the improved nanotube surface ordering in the organic electrolyte, compared with the rough ordering of the aqueous electrolyte.

solution, etches were only attempted at 60 volts)

3.3 Discussion

Reports suggested that an initial electrochemical polish in perchloric acid can be used to reduce surface roughness and improve nanotube ordering, however in-house experiments showed negligible improvement in final nanotube morphology. Perchloric acid is an extremely hazardous chemical, and its use should be avoided whenever possible.

Solution #	F source	Solvent	H$_2$O	Voltage range (V)
1	0.1 mol KF	Aqueous	x	10-30
2	0.3 wt% KF	Ethylene Glycol	3 vol%	40-120
3	0.3 wt% KF	Ethylene Glycol	2 vol%	40-120
4	0.25 wt% NH$_4$F	Ethylene Glycol	0 vol%	40-120
5	0.25 wt% NH$_4$F	Ethylene Glycol	2 vol%	40-120
6	0.27 M NH$_4$F	Formamide	5 wt%	60*

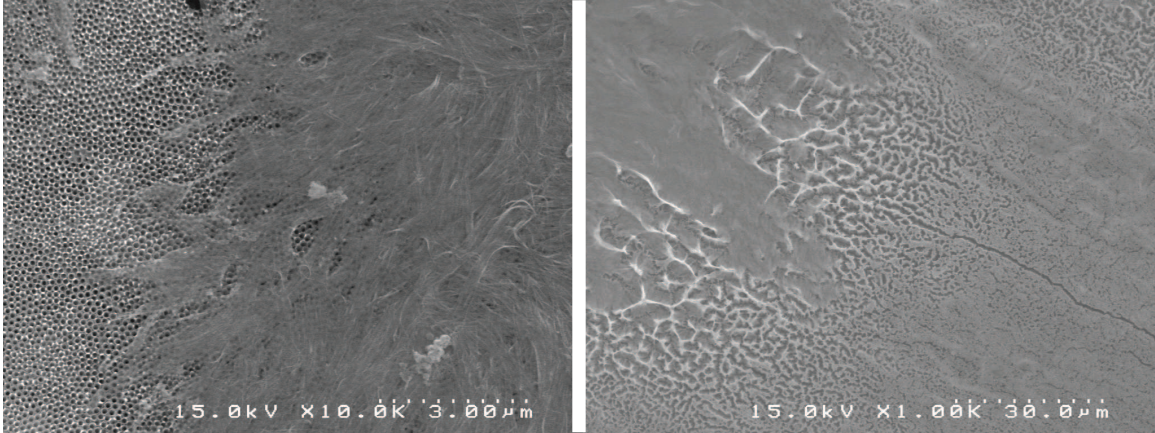Table 3.1: Aqueous and Organic Electrolyte Solutions

Figure 3.5: Nanotube surface debris. Mild sonication in ethanol following the etch removes this debris.

3.3.1 Problems Encountered During Anodization

Nanotube Surface Debris

One of the first problems encountered in optimizing the anodization process was the presence of tube-like debris on the surface of the nanotube array. Figure 3.5 shows an SEM image of this type of surface debris with a clear tube-like form. This was likely to be tubes that had been broken off and settled on top of the tube layer. To clear them off a simple post-etch sonication in ethanol was performed. The post-etch wash needed to be performed before the anneal, otherwise the surface debris would crystallize and remain bound to the substrate.

Particulate TiO$_2$ Debris

A successful anodization would have a characteristic gold color over the surface of the film, which tended to deepen following the anneal step. Occasionally, the film would turn a blue-white color. SEM analysis of these films indicated that this was due to the nanotubes being obscured by non-ordered film of TiO$_2$ coating the surface. It is unknown what ultimately contributed to this film, however, it was found that by using fresh solutions its occurance could be minimized. There is likely no way to

33

prevent this other than careful handling of the sample during the etch process. The best films would keep a characteristic gold shine to them throughout the process, prior to nanocrystal deposition.

3.3.2 Anodization Mechanics

The anodic formation of TiO_2 nanotubes is similar to that of porous aluminum oxide, Al_2O_3. Competing processes at the metal-oxide interface and oxide-electrolyte interface reach a steady state evolution, while chemical etching initiates the formation of pores. Individual pores form at an equal rate with the space defined outside the pore wall, yielding individually distinct nanotubes. This discussion of anodization mechanics is primarily due to Grimes *et al.*[22;30]

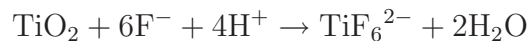A cartoon illustrating the process of nanotube formation is given in Figure 3.6. When the anodizing potential is applied, oxygen ions (O^{2-}) in the electrolyte migrate under the influence of the electric field towards the titanium anode, where they interact with titanium ions (Ti^{4+}) to build up an initial oxide layer at the metal surface. The surface oxidation reactions for an aqueous electrolyte is described by:

$$H_2O \rightarrow O_2 + 4e^- + 4H^+$$

$$Ti + O_2 \rightarrow TiO_2$$
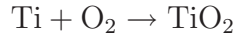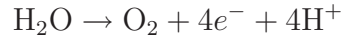
As the oxide layer grows, polarization of the Ti-O bond leads to a uniform field-assisted dissolution of the oxide layer. The Ti^{4+} ions dissolve into the electrolyte, while the O^{2-} ions move towards the metal-oxide interface. In this way, the oxide layer continues to deepen as voltage is applied. Localized pits at the oxide layer surface form as a result of chemical interaction with the fluorine-containing electrolyte. These sites serve as pore forming centers. The reaction can be represented as:

$$TiO_2 + 6F^- + 4H^+ \rightarrow TiF_6{}^{2-} + 2H_2O$$

Clean Ti foil

TiO$_2$

Ti

Surface Oxidation

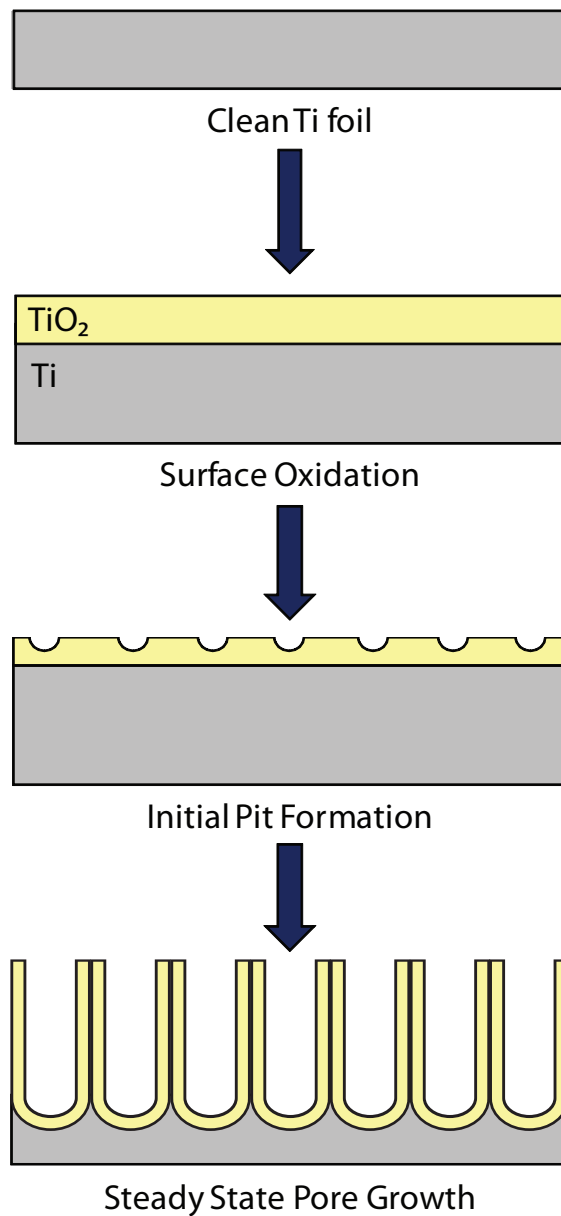Initial Pit Formation

Steady State Pore Growth

Figure 3.6: Cartoon of TiO$_2$ anodization process. Upon application of an external potential, an initial oxide layer is built up, upon which small pits form by a fluorine etch. These pits widen into pores and a steady state process of deeping oxide layer is balanced by the deeping of the pores due to fluorine etching.

Within these pits, the shallower oxide layer will cause an increase in the field-assisted dissolution, causing the pits to grow and form pores. The chemical dissolution is the key to nanotube growth, as it maintains localized field-assisted dissolution at the pore bottoms, allowing the tubes to grow in length. Eventually, a steady-state is reached where oxide growth at the oxide-metal interface is exactly balanced by oxide dissolution at the oxide-electrolyte interface.

Mechanics of Narrowing Nanotubes

SEM characterization revealed an interesting feature of the nanotube array that can be understood using this mechanistic model. The nanotube wall begins to thicken as the tube deepens, narrowing the nanotube pore. See Figure 3.7 for an example where the sample has been fractured in a step-like pattern. This suggests that flow through application may be more difficult. Mechanically, this can be understood as related to the fact that the deeper down the pore you go, the less time there is to etch horizontally into the pore wall, which is a process that occurs at a steady rate and is not field assisted. In that sense the cartoon in Figure 3.6 is slightly disingenuous, in that the tube wall thickness is not fixed from the outset, but rather grows throughout the duration of the etch. It is likely that the distance between pit sites carries some dependence on anodization parameters, which is what gives rise to differing nanotube diameters. Different wall thickness are then due to different horizontal etch rates.

3.4   Thin Film Anodization

Anodization of thin films of titanium, $300 - 400\,\text{nm}$ thick and deposited via RF-sputtering onto FTO coated glass slides, has been reported.[26] The anodization is monitored and stopped when the titanium layer has been completely anodized. When annealed, the nanotube layer turns transparent. This allows a frontside illuminated device architecture in which light enters through the electron-conducting layer.[31]
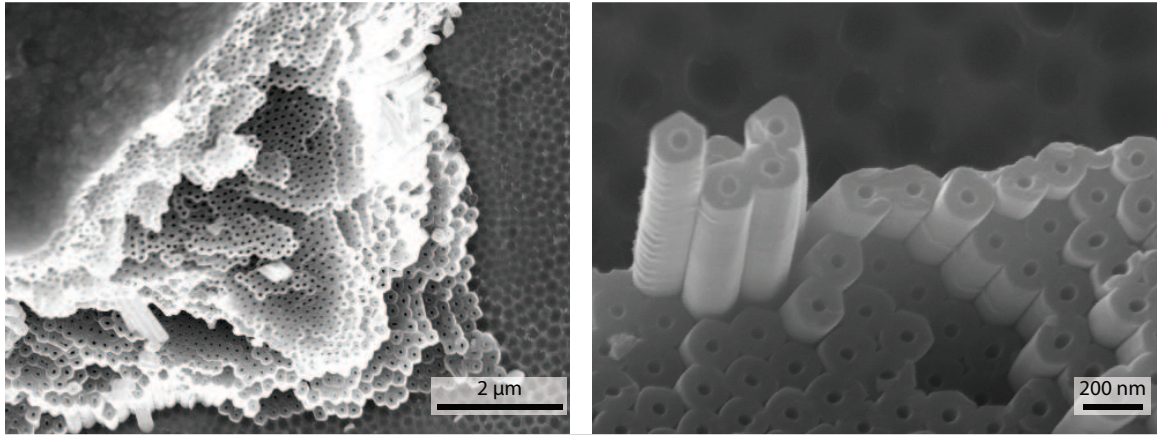
Figure 3.7: Narrowing pores. Left panel shows a fractured sample with a step-like pattern, clearly showing the thickening wall as the tube deepens. Right panel shows a close up of the nanotube near the substrate, showing a much thicker wall than on the surface.

The nanotube layer is sensitized with nanocrystals and filled with polymer, as in the standard device, however now a metal electrode is evaporated onto the back for hole transport. This device structure would require less light to pass through the polymer layers, allowing more light to be harvested by the nanocrystal layer. This section reports on the attempt to fabricate transparent films of TiO_2 nanotube arrays on conducting glass slides. Early tests suggest that with further optimization, such transparent films may be easily fabricated.

300 nm layers of titanium were deposited onto an ITO coated glass slide via electron-beam deposition. Anodization was attempted using standard conditions with an organic electrolyte. It was observed that within minutes of the voltage being applied, the titanium layer had been completely etched away and the area exposed to the electrolyte was transparent. A photograph of such a sample is provided in Figure 3.8. It was initially believed that the titanium layer had been completely etched off the substrate, however examination in the SEM showed a distinct nanoporous TiO_2 structure on the sample.

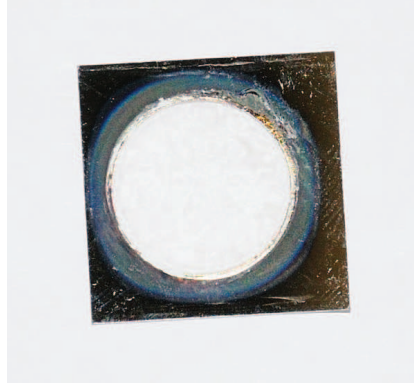Figure 3.9 shows a plan view SEM of an anodized titanium thin film. As can

Figure 3.8: Thin Film TiO$_2$ Anodization - Photograph.

be seen, there is a clear porous nanostructure, however individual nanotubes are not observed at the surface. The profile view, in Figure 3.10, further elucidates the structure. There appears to be formation of discrete nanotubes during the etch, however they remain poorly formed and with significant defects. One possible explanation for this result is that, in the early stages of the etch, field-assisted oxide formation and dissolution dominate over the chemically-assisted pore formation and growth. If the initial titanium layer is too thin, the metal layer may completely oxidize and dissolve before the chemical etch has time to achieve a steady state growth rate. The deposition of thicker layers of titanium would prevent this problem; however properties of titanium make traditional methods of deposition difficult. Alternatively, by reducing the applied potential, it should be possible to slow the formation of the oxide layer and reduce field-assisted dissolution, allowing the pore formation process to occur at a slow rate.
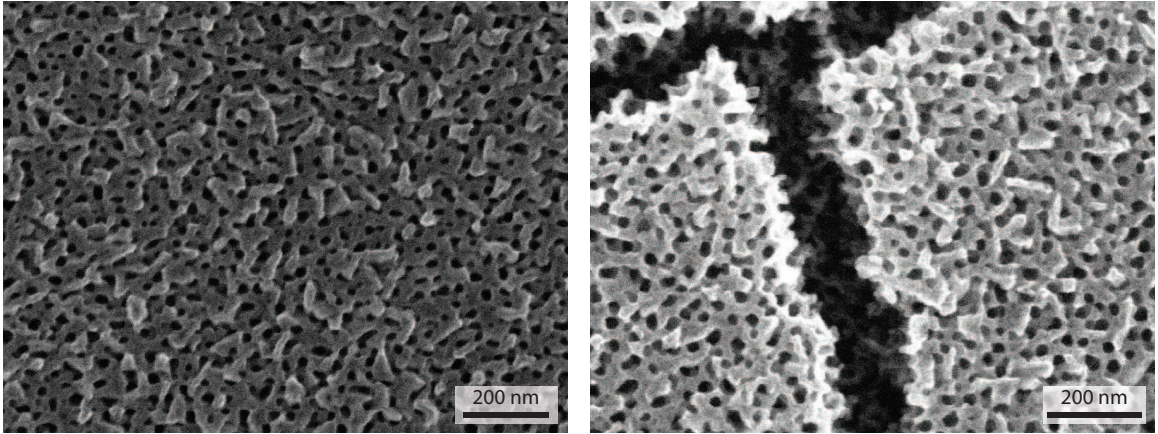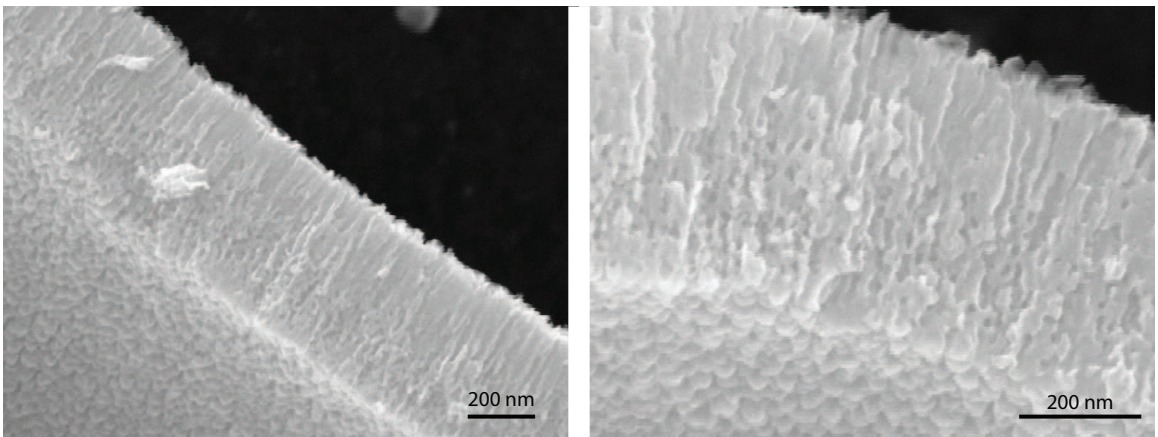
Figure 3.9: Thin Film TiO$_2$ Anodization SEM - Plan View

Figure 3.10: Thin Film TiO$_2$ Anodization SEM - Profile View

FABRICATION AND CHARACTERIZATION OF A NANOCRYSTAL SENSITIZED PHOTOVOLTAIC

4.1   Introduction

This chapter discusses the integration of TiO$_2$ nanotube arrays, described in the previous chapter, with CdSe nanocrystals and conjugated polymers to form a solid-state, ordered heterojunction photovoltaic device. Section 4.2 summarizes the deposition of nanocrystals onto the TiO$_2$ electrode. Section 4.3 describes the deposition of conjugated polymer layers and the finalization of device construction. Section 4.4 presents results of testing and characterization of the device.

4.2   Nanocrystal Deposition

Of the three deposition techniques attempted, chemical linking proved to be the most robust; however electrophoretic deposition (EPD) presents a promising alternative. Neither drop casting nor immersion was successful in permanently linking nanocrystals to pore walls.

4.2.1   Drop Cast and Immersion

Successful binding without a linking intermediate would require a strong electrostatic force between the nanotube wall and the nanocrystal. Sample fluorescence indicated nanocrystal deposition onto the surface. However, when the samples were scraped from the substrate and deposited into a 2-propanol solution and sonicated to prepare for TEM imaging, the nanocrystals, evidenced by their fluorescence, settled at the bottom of the solution, while the TiO$_2$ remained in solution. This indicates that both drop cast and immersion do not result in the nanocrystals binding well
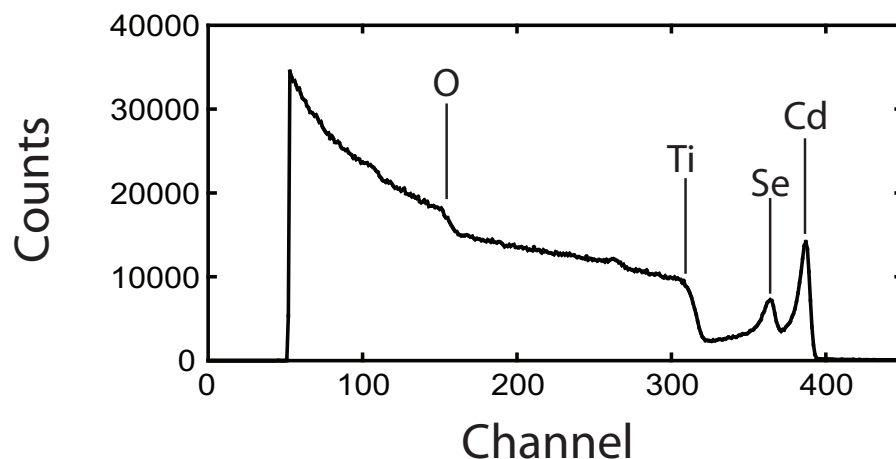
Figure 4.1: RBS Spectra for Chemically Linked CdSe Nanocrystals

to the surface of the TiO_2 electrode. A method to more strongly functionalize the surface and actively bind the nanocrystals is necessary.

4.2.2 Chemical Linking

Elemental analysis confirms deposition of CdSe nanocrystals via chemical linking. No difference was observed between samples immersed in the nanocrystal solution for 12 hours and those for 96 hours. An RBS spectra is provided in Figure 4.1. A complimentary EDS spectra is provided in Figure 4.2. Further work should utilize RBS to perform depth-resolved elemental composition to determine how deeply nanocrystals have penetrated into the TiO_2 nanotube layer. Lacking this data, the depth and uniformity of nanocrystal coverage in the TiO_2 nanotubes is not fully characterized.

Electron microscopy confirms surface functionalization. TEM imaging shows nanocrystals linked to the inner surface of the nanotubes, further confirming successful deposition (Figure 4.3). The TEM image suggests that nanocrystals aggregate along the surface of the nanotube wall in a nearly monolayer fashion. Regions of clumping are visible, and are likely due to excess organic ligands on the surface of
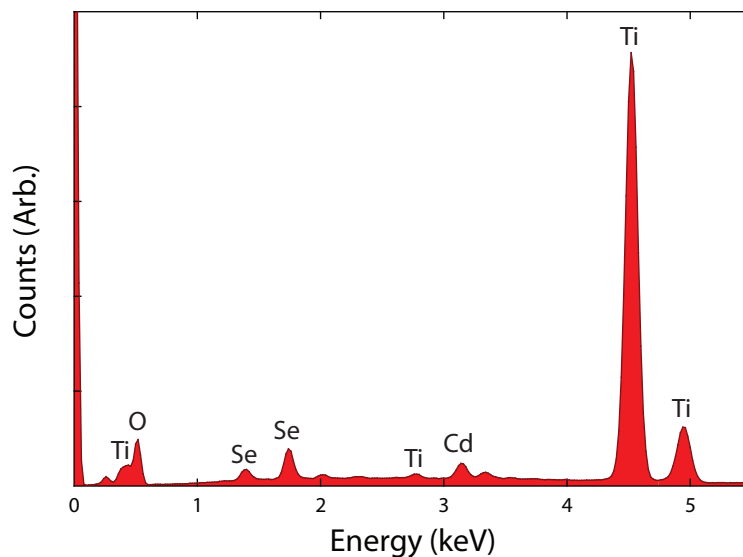
Figure 4.2: EDS Spectra for Chemically Linked CdSe Nanocrystals

individual nanocrystals binding together. A more thorough washing step following chemical linking should be sufficient to disassociate these nanocrystals. SEM images also confirm deposition (Figure 4.4). The SEM images show nanocrystals forming a uniform coating along the nanotube walls. The nanocrystal layer appears somewhat fuzzy, and individual nanocrystals cannot be resolved. We attribute this both to the limited resolution of the SEM, and the presence of excess organic ligands deposited along with the nanocrystals. As noted earlier, SEM imaging was only capable of demonstrating nanocrystals on the outside of nanotube walls. TEM imaging confirmed deposition within the nanotubes.

4.2.3 Electrophoretic Deposition

EPD was also successful in depositing nanocrystals onto the TiO_2 surface, as can be seen from the EDS spectrum collected in Figure 4.5. EDS spectra are obtained from operating the Hitachi SEM in EDS mode. While EPD presents an impressive alternative to the time intensive process of chemical linking, we have found it limited in that the success of a deposition is highly dependant on the quality and cleanliness of

Figure 4.3: TEM of CdSe nanocrystals chemically linked to the inside wall of a TiO_2 nanotube. The large dark portion is the nanotube wall, along which individual nanocrystals can be resolved.
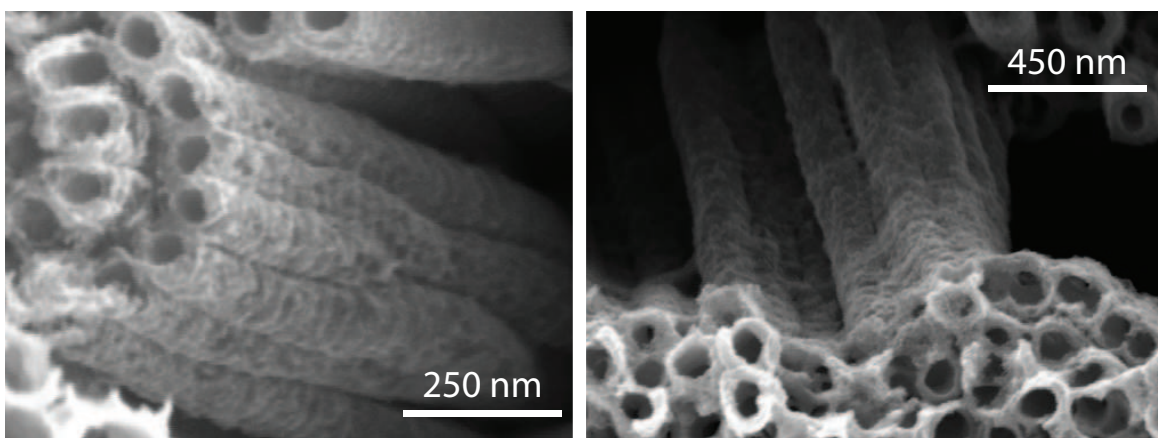

Figure 4.4: SEM of CdSe nanocrystals chemically linked to TiO_2 nanotubes
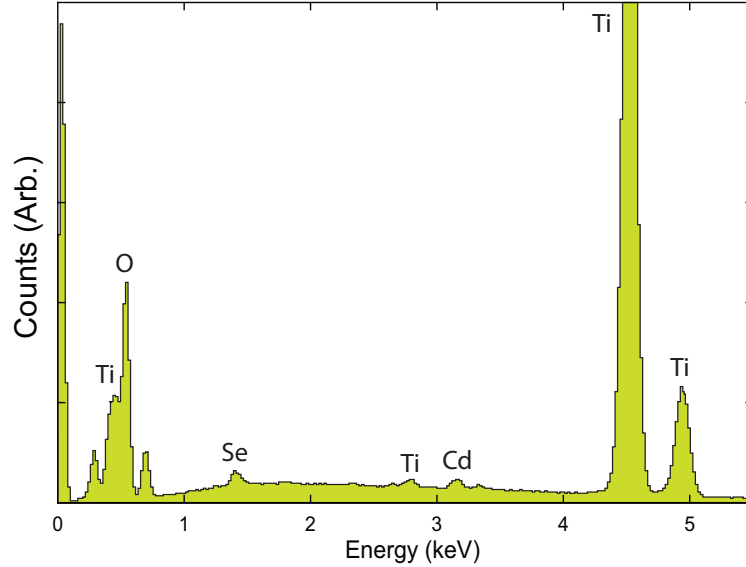
Figure 4.5: Energy-Dispersive X-Ray Spectroscopy (EDS) results for CdSe nanocrystals electrophoretically deposited onto TiO_2 nanotubes. Cadmium and selenium peaks are labeled following auto-id.

the nanocrystal sample to be deposited. At this point in time, more work is necessary to understand the kinetics of the EPD process to make it a viable option for a wider range of nanocrystal preparations.

SEM images of nanocrystals deposited on TiO_2 nanotube films via EPD suggest that the nanocrystals are unable to penetrate into the nanotube layer. Rather, nanocrystals tend to pile up on the surface of the nanotube, blocking access to the pores. Future experiments should explore EPD in more depth, and determine whether varying the parameters (voltage, etc.) will allow for slower deposition and minimize pore blockage.

4.3   Device Construction

Following nanocrystal deposition, the next step in device construction involved the pentration of a conjugated polymer layer into the nanotube film. The method employed consisted in first spin-casting a layer of TPD onto the nanotube film, then
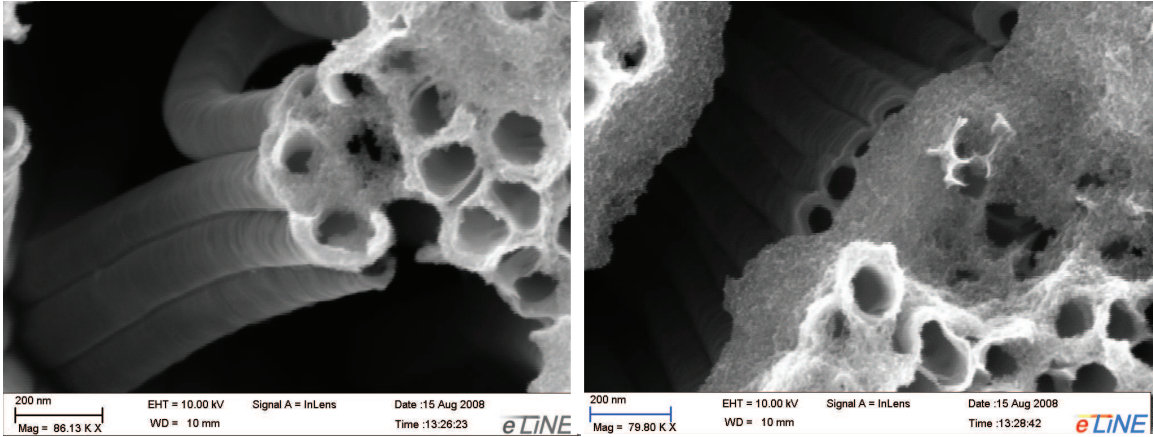
Figure 4.6: SEM images of CdSe nanocrystals electrophoretically deposited on TiO$_2$ nanotubes.

annealing at $100\,^\circ$C to drive the polymer into the pores. This was repeated with a film of PEDOT:PSS. The final anneal was conducted at very high temperature to facilitate pore penetration. These two polymers were chosen because of their well characterized electronic properties and air stability. TPD has been largely deployed in organic electroluminescent devices, and some reports have shown it to be effective in heterojunction photovoltaic devices.[32] Alternative conjugated polymers, such as poly-3-hexylthiophene (P3HT) and poly[2-methoxy-5-(2'-ethylhexyloxy)-p-phenylene vinylene] (MEH-PPV), have found more widespread application in photovoltaic devices because of their high absorption coefficients.[33] However, even in processed form these materials are extremely air senstitive and cannot form the stable devices desired for this study.

The effectivenes of pore penetration cannot be determined using nondestructive techniques. Hence it is unknown how well the polymer layer is capable of penetrating into the nanotube layer. Plan-view SEM images, shown in Figure 4.7, show that the polymer layer is capable of penetrating the nanotube layer, essential for ensuring good interfacial contact with the ITO top contact. Figure 4.8 shows a profile view SEM image of which suggests that the polymer layer does not penetrate deeply
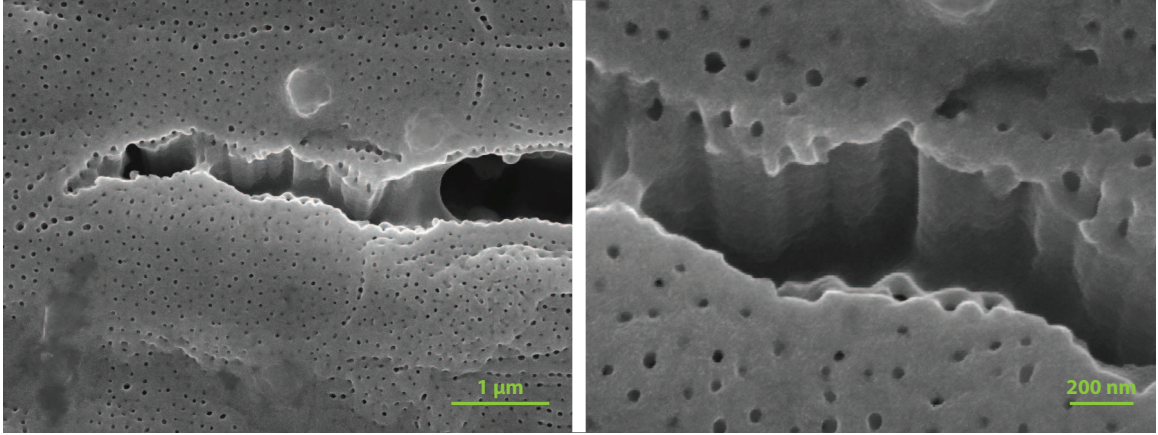
Figure 4.7: SEM of TiO$_2$ nanotubes following polymer deposition. Two plan views.

into the pores. The polymer layer appears as one continuous film draped over the nanotube layer. It is likely that spin-casting the initial layer does not deposit a sufficient quantity of polymer onto the nanotube surface to ensure complete penetration and heterojunction formation. Typical spun-cast polymer layers are on the order of $20 - 30\,\text{nm}$, while nanotube films are generally microns long, implying that the increased surface area is not fully coated. Figure 4.9 shows an additional profile view of the deposited polymer layer, indicating that the polymer may indeed be coating the nanotube walls. These conflicting images suggest further experimentation is necessary to determine the nature of polymer deposition into the nanotubes. Multiple coatings were attempted, however showed negligible improvements in device performance. Alternative techniques of polymer deposition that should be investigated include simple drop-casting and a more complex, but possibly controllable, thermal evaporation. However, it remains to be seen if thermal evaporation is capable of effectively penetrating pores.

No attempt was made in this study to deposit solution-processed ITO onto the constructed device, fearing that the high temperature anneal required to acheive high conductivity in the ITO film would result in destruction of the CdSe and polymer layers. Instead, a sandwich approach was adopted, in which the ITO layer was simply
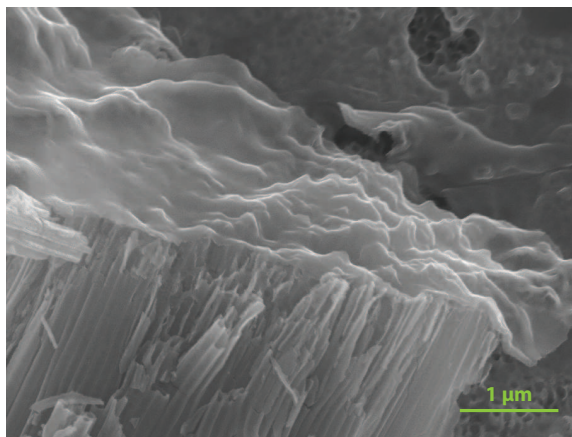
Figure 4.8: SEM of TiO$_2$ nanotubes following polymer deposition. Profile view makes it appear that the polymer layer does not penetrate deeply into the pores.
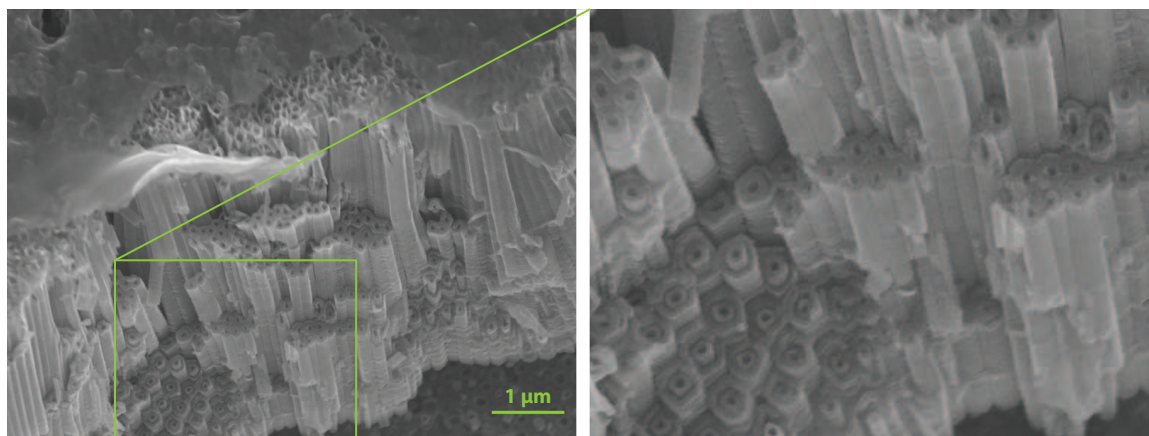
Figure 4.9: A second SEM view of TiO$_2$ nanotubes following polymer deposition in profile. Judging from a view of the top of the nanotube layer, the polymer does not penetrate. However, the zoom-in view clearly indicates a dual layer nanotube, suggesting a layer of coating. Collection of TEM images further elucidating the internal structure of the nanotubes are currently being collected.

pressed against the functionalized TiO_2 and polymer layer. This device architecture has precedent, and has been used in organic device to achieve respectable conversion efficiencies.[29] However, this architecture is clearly not ideal and can only be considered an interim measure prior to development of a complete fabrication procedure.

To improve electrical contact between the ITO and the PEDOT:PSS coated TiO_2 layer, a thin film of PEDOT:PSS was first spun-cast onto the ITO slide. The two electrodes were pressed together and maintained in contact using a binder clip, following standard procedures for photoelectrochemical devices. An attempt was made to heat seal the electrodes in the furnace at $120\,°C$, however this was unsuccessful. An alternative method, sealing the two electrodes under higher vacuum, has been suggested but not attempted.

To summarize: the final working device consists of an anodized TiO_2 nanotube array sitting on a titanium foil, and functionalized with CdSe nanocrystals. A heterojunction is formed by infiltrating the nanotubes with a hole-conductive polymer, TPD, followed by a processed layer of PEDOT:PSS. Finally, a patterned ITO slide, coated with PEDOT, is sandwiched against the titanium foil and secured in place. The working device is stored in air and tested devices have remained stable over a six month testing period. A photograph of a finalized device is provided in Figure 4.10

4.4 Device Characterization

Under illumination from the simulated solar spectrum, devices showed a photovoltaic response. Devices were tested under solar-spectrum illumination of a $50\,W$ Solux 4700K lamp with an average incident power intensity of $10\,mW/cm^2$ at room temperature in atmosphere. The device photovoltage-current response curve is shown in Figure 4.11, which reflects the most responsive device, but is typical of successfully fabricated devices. Figures of merit for this device are as follows: $J_{sc} = 6.33\,\mu A/cm^2$, $V_{oc} = 535\,mV$, $\eta = 0.015\%$, $FF = 0.39$. This device architecture represents an im-
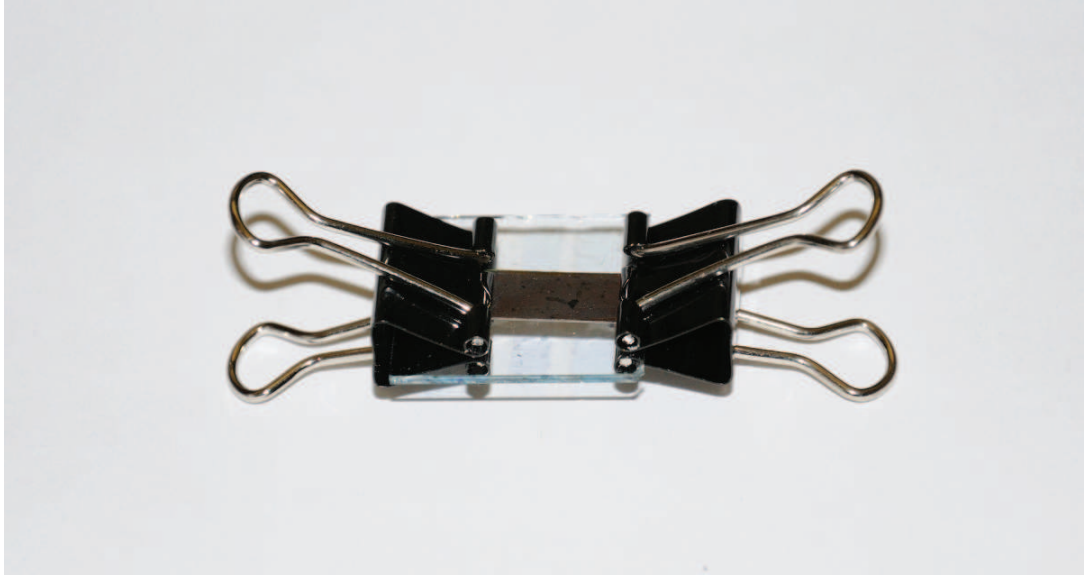
Figure 4.10: Device Photograph.

provement of four orders of magnitude over our previously reported device, which utilized electrophoretically deposited CdSe on planar films of TiO_2.[7] We attribute this improved efficiency to the increased surface area available for nanocrystal sensitizatation due to the nanotube architecture. A control sample lacking nanocrystals produced a photovoltaic response with an efficiency of $10^{-7}\%$, as expected from the energy band diagram in Figure 1.5. However, the nanocrystals greatly enhance the quantum efficiency of the device, significantly increasing the device photocurrent by acting as light harvesting centers.

Tested device efficiencies remain lower than comparable quantum dot devices using liquid electrolytes. We attribute this to several factors: poor interfacial coupling between the nanocrystals and the TPD layer, incomplete penetration of nanocrystals into the nanotube layer, and poor ITO contact with the PEDOT:PSS layer. It is likely that gas molecules present within the nanotube pores prevent full access by the nanocrystal solution to the increased electrode surface area. Pore penetration by conjugated polymer chains remains to be fully characterized.

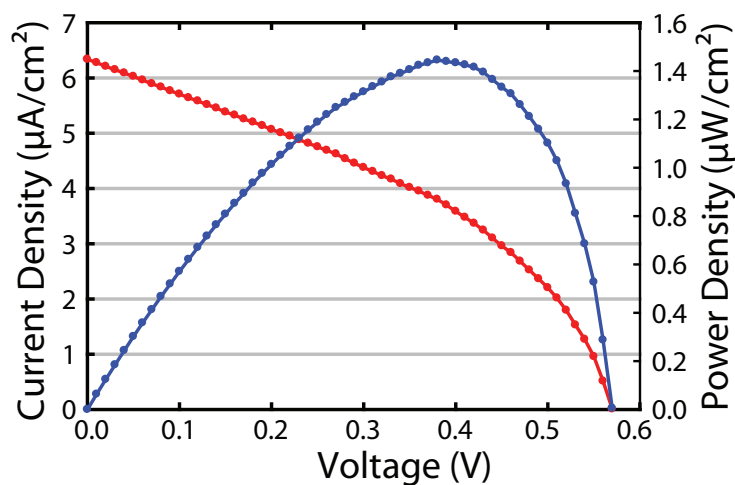Figure 4.11: Photocurrent-voltage response of the nanocrystal sensitized device shown in red. Power conversion efficiency shown in blue. Peak power conversion efficiency of 0.015% occurs at V=0.39 V.

Low device fill factor is likely due to a high shunt resistance in the device stemming from incomplete formation of the heterojunction layer. Regions within the TiO$_2$ nanotube pores that are not coated with active nanocrystals but are in contact with the polymer layer increase this resistance. Organic ligands present may act as a barrier against contact between the TiO$_2$ and the TPD, however there is no efficient way of controlling the presence of the organic ligands. It is likely that an active layer several nanocrystals thick will be necessary to ensure good interface formation, however the current sensitization technique allows for only single monolayer deposition. Further improvements in the processing of hole transport layers will be required before device efficiencies can be improved. A recent report has indicated that thermal evaporation of the TPD layer may be an alternative to spin-casting, however it is unknown whether this technique will allow for efficient pore infiltration.[34] Experiments aimed at eliminating the polymer layers entirely, in favor of direct contact with the ITO layer, are currently in progress.

As fabricated, these devices are frontside illuminated, with light passing through

50

the hole conducting layers prior to reaching the nanocrystals. A significant source of efficiency losses can be attributed to the high absorption coefficient of the polymer layers restricting photon absorption by the nanocrystals. Backside illuminated polymer devices consisting of TiO_2 nanotubes grown on FTO-doped glass slides have shown improved properties over frontside illuminated devices.[31]

CHAPTER V

CONCLUSIONS AND FUTURE DIRECTIONS

5.1 Conclusions

This thesis described the fabrication of a novel photovoltaic device employing semiconductor nanocrystals as sensitizing light harvester, and ordered arrays of TiO_2 nanotubes as the electron conducting layer. Nanocrystals were sensitized to the TiO_2 surface via a bifunctional linking molecule. A device efficiency of 0.015% was demonstrated using a sandwich device construction and conjugated polymers as hole transport layers. One significant source of efficiency loss is the poor electronic contact between the polymer layers. Processing of conjugated polymers needs to be improved significantly. A new device architecture that constructs the device in one single layer is also required in order to improve the electrical interface and minimize losses in the polymer layers. However, this project has shown that semiconductor nanocrystals remain a promising candidate for advanced photovoltaics.

5.2 Future Directions

Future directions should be focused on developing alternative device architectures that do not require a sandwich construction, and can instead be fabricated entirely on a single substrate. Several potential approaches for this are detailed below.

5.2.1 Free Standing TiO₂ Nanotubes

Devices based on the anodization process described in this thesis are limited by the fact that the TiO_2 layer is formed on a titanium substrate. Removing the TiO_2 layer from the titanium substrate would increase the flexibility in constructing new

device architectures. The devices in this study are limited to backside-illuminated only. Efforts to fabricate nanotubes on ITO substrates were unsuccessful.

Recent reports have demonstrated that it should be in principle possible to remove the TiO_2 nanotube layer from the underlying metal substrate through either a peel-off technique or an acid etch. The benefits of this would be two-fold: (1) increased flexibility in constructing device architecture. The nanotube layer could be set onto a TCO substrate or onto an aluminum substrate, whose band features are more precisely optimized for heterojunction formation. (2) The fabrication of a free-standing nanotube layer opens the possibility of nanotubes that are open on both ends. Once removed, the closed end of the nanotube layer could be selectively etched away, opening the bottoms of the pores and resulting in entirely open nanotubes. This would increase flexibility in depositing nanotube, as capillary forces and air pockets would not have to be contended with when attempting to deposit nanocrystals. A technique exploiting this is described below.

5.2.2   *Flow-through Nanocrystal Deposition*

An immediate idea that arises from considering free-standing films of open-ended TiO_2 nanotubes is a flow through nanocrystal deposition. A dilute solution of nanocrystals in solvent could be passed through the nanotube layer. Either the nanocrystals, or the nanotubes, could be chemically functionalized with the linking molecule MPA, in order to faciliate binding onto the surface. The nanocrystal solution could be passed through the nanotube layer under either an electric or pressure gradient in order to assure the nanocrystals do not clog the surface. Here the scale of our nanotubes would be advantageous, as it would ensure adequate flow through. Reports have demonstrated that it is possible to fill pores on the order of our nanotube diameters, so it should not present a problem to flow through the solution. The difficulty to be overcome would be ensuring that the nanocrystals are adequately bound

to the surface. One can imagine changing the angle of the nanotube film within the solution in order to push the nanocrystals towards the walls of the nanotubes in all directions.

5.2.3   Pulsed laser deposition of ITO electrode

Most significantly, new techniques of forming the hole transport layer are required. Fabrication of an entirely inorganic device will require a technique of directly depositing ITO films to replace the polymer layers currently in use. One technique of promise is pulsed laser deposition (PLD), which has been shown capable of depositing thin films of ITO at low temperature. Further study is necessary to see if PLD can allow for efficient nanotube penetration by the ITO and formation of heterojunction contact.

APPENDIX A

SYNTHESIS OF PBSE NANOCRYSTALS

A.1   Introduction

The devices fabricated in this thesis employed standard CdSe nanocrystals as the light harvesting element. CdSe has a relatively large bulk band gap $E_g = 1.73 \, \text{eV}$, corresponding to an absorption edge at approximately $\lambda = 708 \, \text{eV}$, in the red portion of the visible spectrum. CdSe does not absorb in the infrared, missing a large fraction of the solar spectrum, making it nonideal for photovoltaic devices. Having established prototype devices using CdSe nanocrystals, practical device development will likely transition to PbSe nanocrystals, which have a bulk absorption edge at $\lambda \approx 2000 \, \text{nm}$, and can absorb much more of the solar spectrum.

Late work in this project considered the synthesis of monodisperse PbSe nanocrystals. This synthesis had been previously conducted in the Rosenthal lab by Danielle Garrett.[35] The synthesis is very similar to that of CdSe nanocrystals, consisting of a PbO precursor and a high-temperature Se:TBP injection. While TEM images showed PbSe nanocrystals, absorption data was not obtained owing to difficulties in dissolving the nanocrystals in an appropriate solvent for UV-VIS-NIR characterization. This appendix briefly outlines the PbSe nanocrystal synthesis and characterization and problems encountered.

A.2   Synthesis

PbSe nanocrystals were pyrolytically synthesized in a one-pot technique following M.D. Garrett[35]. A standard synthesis consisted of a 1:1 Pb:Se precursor ratio. Briefly, 0.45 g PbO, 4.0 mL ODE, and 7.5 g OA were combined in a three neck flask,

stirred and purged under argon. The sample was heated to 180 °C, at which point the solution turned from yellow to clear as the lead oxide converted to lead oleate. The sample was held at this temperature for 30 minutes to allow for complete dissolution of the PbO precursor.[36] Occasionally, the PbO would not entirely convert and small yellow pellets would be observed in the solution. Raising the temperature to 240 °C was generally successful at converting the pellets. After conversion, the temperature was reduced to 165 °C and 2.5 mL 1 M Se:TBP was rapidly injected. Upon injection the temperature dropped to 150 °C and the solution immediately turned dark. The solution was held at 150 °C to allow nanocrystal growth.

A.3 Cleanup

The PbSe nanocrystals were recovered using an acetone-chloroform extraction. A small amount of chloroform is added to help make the oily precursors miscible in the acetone. Centrifugation crashes out the nanocrystals, which were then dried and redispersed in an appropriate solvent.

Several problems were encountered in the cleanup. First, often following a first extraction cycle, a two-phase precipate was observed. It was conjectured that this was likely excess precursors that did not remain in the acetone solution, however further cycles were unable to reduce their presence without severely impacting nanocrystal yield. Second, and more importantly, redispersion in a solvent appropriate for UV-VIS-NIR characterization was unsuccessful. With vibrational absorption features in the NIR, standard solvents are too noisy to yield a signal-free background. Tetrachloroethylene (TCE) is commonly used as a spectroscopic solvent, however all attempts to dissolve the nanocrystals in TCE failed. The nanocrystals were observed to form a muddy solution and slowly flocculate out of solution. Earlier samples of PbSe stored in TCE (from M.D. Garrett) also flocculated upon dilution. This is in contrast to other reported PbSe preparations, all of which have used TCE as a
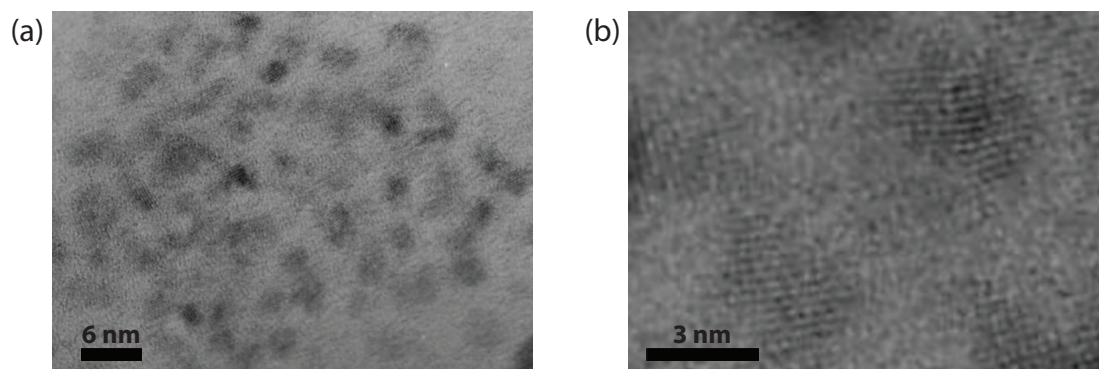
Figure A.1: TEM images of PbSe Nanocrystals. (a) Macroview showing relatively poor size distribution. (b) Closeup of PbSe fringes.

spectroscopic solvent without issue.[36–39]

A.4 Characterization

Figure A.1 shows TEM micrographs of PbSe nanocrystals with poor size distribution.

UV-VIS-NIR absorption spectroscopy is necessary to determine the fundamental absorption edge, and hence band gap, of the nanocrystal sample. Difficulties dispersing samples in TCE prevented collection of conclusive spectra. A sample spectra taken in chloroform is provided in Figure A.2, showing no distinguishable features. However, the absorption onset begins to rise at wavelengths greater than 1000 nm, consistent with expectations for a broadly dispersed PbSe nanocrystal sample. A reliable synthesis for monodisperse PbSe nanocrystals is still sought.
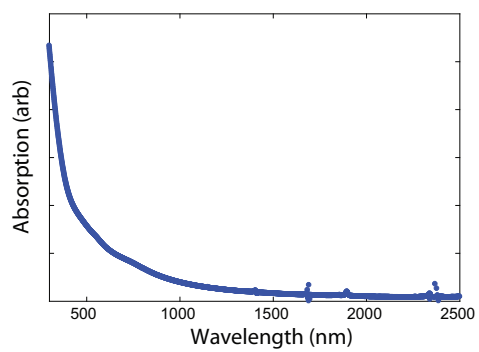
Figure A.2: PbSe nanocrystal absorption spectra obtained in chloroform solvent.

REFERENCES

[1] Intergovernmental Panel on Climate Change, *Climate Change 2007: Synthesis Report*; Technical Report 4, 2007.

[2] Lewis, N. S.; Nocera, D. G. *Proceedings of the National Academy of Sciences of the United States of America* **2006**, *103*, 15729–15735.

[3] Basic Energy Sciences Workshop on Solar Energy Utilization, *Basic Sciences Needs for Solar Energy Utilization*; Technical Report, 2005.

[4] Bowers, M. J.; McBride, J. R.; Rosenthal, S. J. *Journal of the American Chemical Society* **2005**, *127*, 15378–15379.

[5] Schreuder, M. A.; Gosnell, J. D.; Smith, N. J.; Warnement, M. R.; Weiss, S. M.; Rosenthal, S. J. *Journal of Materials Chemistry* **2008**, *18*, 970–975.

[6] Swafford, L.; Rosenthal, S. J. Molecular and Nanocrystal Based Photovoltaics. In *Molecular Nanoelectronics*; Reed, M. A., Lee, T., Eds.; American Scientific Publishers, 2003.

[7] Smith, N. J.; Emmett, K. J.; Rosenthal, S. J. *Applied Physics Letters* **2008**, *93*, 043504.

[8] Kamat, P. V. *The Journal of Physical Chemistry C* **2008**, *112*, 18737–18753.

[9] Michalet, X.; Pinaud, F. F.; Bentolila, L. A.; Tsay, J. M.; Doose, S.; Li, J. J.; Sundaresan, G.; Wu, A. M.; Gambhir, S. S.; Weiss, S. *Science* **2005**, *307*, 538–544.

[10] Warnement, M.; Tomlinson, I.; Rosenthal, S. *Current Nanoscience* **2007**, *3*, 273–284.

[11] Rosenthal, S. J.; Tomlinson, I.; Adkins, E. M.; Schroeter, S.; Adams, S.; Swafford, L.; McBride, J.; Wang, Y.; DeFelice, L. J.; Blakely, R. D. *Journal of the American Chemical Society* **2002**, *124*, 4586–4594.

[12] Fox, M. *Optical Properties of Solids*; Oxford University Press: Oxford, 2001.

[13] Ashoori, R. *Nature* **1996**, *379*, 413–419.

[14] Shockley, W.; Queisser, H. J. *Journal of Applied Physics* **1961**, *32*, 510–519.

[15] Schaller, R. D.; Sykora, M.; Pietryga, J. M.; Klimov, V. I. *Nano Letters* **2006**, *6*, 424–429.

[16] O'Regan, B.; Grätzel, M. *Nature* **1991**, *353*, 737–740.

[17] Gratzel, M. *Philosophical Transactions of the Royal Society A-Mathematical Physical and Engineering Sciences* **2007**, *365*, 993–1005.

[18] Nozik, A. *Physica E-Low-Dimensional Systems & Nanostructures* **2002**, *14*, 115–120.

[19] Zhu, K.; Neale, N. R.; Miedaner, A.; Frank, A. J. *Nano Letters* **2007**, *7*, 69–74.

[20] Sukhovatkin, V.; Hinds, S.; Brzozowski, L.; Sargent, E. H. *Science* **2009**, *324*, 1542–1544.

[21] Goh, C.; Coakley, K. M.; McGehee, M. D. *Nano Letters* **2005**, *5*, 1545–1549.

[22] Grimes, C. A. *Journal of Materials Chemistry* **2007**, *17*, 1451–1457.

[23] Prakasam, H. E.; Shankar, K.; Paulose, M.; Varghese, O. K.; Grimes, C. A. *The Journal of Physical Chemistry C* **2007**, *111*, 7235–7241.

[24] Rosenthal, S. J.; McBride, J.; Pennycook, S. J.; Feldman, L. C. *Surface Science Reports* **2007**, *62*, 111–157.

[25] Yu, W.; Qu, L.; Guo, W.; Peng, X. *Chemistry of Materials* **2003**, *15*, 2854–2860.

[26] Mor, G.; Varghese, O.; Paulose, M.; Grimes, C. *Advanced Functional Materials* **2005**, *15*, 1291–1296.

[27] Robel, I.; Subramanian, V.; Kuno, M.; Kamat, P. *Journal of the American Chemical Society* **2006**, *128*, 2385–2393.

[28] Gurrappa, I.; Binder, L. *Science and Technology of Advanced Materials* **2008**, *9*, 043001.

[29] Mor, G. K.; Shankar, K.; Paulose, M.; Varghese, O. K.; Grimes, C. A. *Applied Physics Letters* **2007**, *91*, 152111.

[30] Mor, G. K.; Varghese, O. K.; Paulose, M.; Shankar, K.; Grimes, C. A. *Solar Energy Materials and Solar Cells* **2006**, *90*, 2011–2075.

[31] Shankar, K.; Mor, G.; Paulose, M.; Varghese, O.; Grimes, C. *Journal of Non Crystalline Solids* **2008**, *354*, 2767–2771.

[32] Arango, A. C.; Oertel, D. C.; Xu, Y.; Bawendi, M. G.; Bulovic, V. *Nano Letters* **2009**, *9*, 860–863.

[33] Huynh, W.; Dittmer, J.; Alivisatos, A. *Science* **2002**, *295*, 2425–2427.

[34] Anikeeva, P. O.; Madigan, C. F.; Halpert, J. E.; Bawendi, M. G.; Bulović, V. *Physical Review B (Condensed Matter and Materials Physics)* **2008**, *78*, 085434.

[35] Garrett, M. D. Ph.D. thesis, Vanderbilt University: Nashville, TN, 2007.

[36] Murphy, J. E.; Beard, M. C.; Norman, A. G.; Ahrenkiel, S. P.; Johnson, J. C.; Yu, P.; Micic, O. I.; Ellingson, R. J.; Nozik, A. J. *Journal of the American Chemical Society* **2006**, *128*, 3241–3247.

[37] Du, H.; Chen, C.; Krishnan, R.; Krauss, T. D.; Harbold, J. M.; Wise, F. W.; Thomas, M. G.; Silcox, J. *Nano Letters* **2002**, *2*, 1321–1324.

[38] Evans, C. M.; Guo, L.; Peterson, J. J.; Maccagnano-Zacher, S.; Krauss, T. D. *Nano Letters* **2008**, *8*, 2896–2899.

[39] Koktysh, D.; McBride, J.; Dixit, S.; Feldman, L.; Rosenthal, S. *Nanotechnology* **2007**, *18*, 495607.